



1 Resolving Vertical Profile of Cloud Condensation Nuclei Concentrations from 2 Spaceborne Lidar Measurements

3 Piyushkumar N. Patel^{1,2,*}, Jonathan H. Jiang¹, Ritesh Gautam³, Harish Gadhavi⁴, Olga V.
4 Kalashnikova¹, Michael J. Garay¹, Lan Gao⁵, Feng Xu⁵, Ali H. Omar⁶

5
6 ¹Jet Propulsion Laboratory, California Institute of Technology, Pasadena, CA, USA

7 ²Oak Ridge Associated Universities, Oak Ridge, TN, USA

8 ³Environmental Defense Fund, Washington, DC, USA

9 ⁴Physical Research Laboratory, Ahmedabad, India

10 ⁵School of Meteorology, University of Oklahoma, OK, USA

11 ⁶Science Directorate, NASA Langley Research Center, Hampton, VA, USA

12

13 *Corresponding Author: Piyushkumar N. Patel, (piyushether@gmail.com,
14 piyushkumar.n.patel@jpl.nasa.gov)

15 **Keywords:** CCN, aerosol, cloud, CALIPSO, satellite, Lidar

16

17 **Abstract.** Cloud condensation nuclei (CCN) are mediators of aerosol-cloud interactions (ACI),
18 contributing to the largest uncertainties in the understandings of global climate change. We present
19 a novel remote sensing-based algorithm that quantifies the vertically-resolved CCN number
20 concentrations (N_{CCN}) using aerosol optical properties measured by a multiwavelength lidar. The
21 algorithm considers five distinct aerosol subtypes with bimodal size distributions. The inversion
22 used the look-up tables developed in this study, based on the observations from the Aerosol
23 Robotic Network to efficiently retrieve optimal particle size distributions from lidar
24 measurements. The method derives dry aerosol optical properties by implementing hygroscopic
25 enhancement factors to lidar measurements. The retrieved optically equivalent particle size
26 distributions and aerosol type dependent particle composition are utilized to calculate critical
27 diameter using the κ -Köhler theory and N_{CCN} at six supersaturations ranging from 0.07% to 1.0%.
28 Sensitivity analyses indicate that uncertainties in extinction coefficients and relative humidity
29 greatly influence the retrieval error in N_{CCN} . The potential of this algorithm is further evaluated by
30 retrieving N_{CCN} using airborne lidar from the NASA ORACLES campaign and validated against
31 simultaneous measurements from the CCN counter. The independent validation with robust
32 correlation demonstrates promising results. Furthermore, the N_{CCN} has been retrieved for the first
33 time using a proposed algorithm from spaceborne lidar - Cloud-Aerosol Lidar with Orthogonal
34 Polarization (CALIOP) - measurements. The application of this new capability demonstrates the
35 potential for constructing a 3D CCN climatology at a global scale, which help to better quantify
36 ACI effects and thus reduce the uncertainty in aerosol climate forcing.



37 1 Introduction

38 The Intergovernmental Panel on Climate Change (IPCC) report states that radiative forcing caused
39 by aerosol-cloud interactions (ACI), dominates the largest uncertainty, and remains the least well-
40 understood anthropogenic contribution to climate change (IPCC AR5, 2013). The uncertainty
41 mainly stems from the complicated processes of how aerosols impact the global cloud system.
42 Atmospheric aerosols allow for water vapor condensation under certain supersaturation (SS)
43 conditions and subsequently evolve into cloud droplets by serving as cloud condensation nuclei
44 (CCN). Anthropogenic emissions are a major source of CCN, facilitating the formation of cloud
45 droplets, thereby altering cloud properties, precipitation patterns, and hence the climate forcing
46 (Carslaw et al., 2010; Paasonen et al., 2013). Consequently, reducing the uncertainty associated
47 with ACI is crucial for increasing our confidence in predictions of global and regional climate
48 models (IPCC, 2014). The fundamental parameter for understanding the aerosol-cloud interaction
49 is the CCN concentrations (Rosenfeld et al., 2014). Determining CCN number concentration
50 (N_{CCN}) is the basis for analyses of ACI (Seinfeld et al., 2016). Large uncertainties in their
51 magnitude and variability at a global scale are one of the main factors for the low level of scientific
52 understanding of ACI effects. Therefore, knowledge of the global abundance of aerosols capable
53 of serving as CCN is fundamental to advancing our understanding of ACI (Fan et al., 2016).

54 Tackling the challenges in climate change, as identified by the IPCC, requires that CCN properties
55 be measured globally. Missing such a fundamental quantity has greatly hindered our ability to
56 accurately quantify the effects of anthropogenic aerosols on cloud properties (Rosenfeld et al.,
57 2014). Ground-based instruments can observe N_{CCN} at various SS, but they only provide sparse
58 and localized information. Besides limited coverage, near-surface CCN properties could differ
59 significantly from CCN properties near the cloud base due to vertical aerosol inhomogeneities,
60 particularly under stable atmospheric boundary conditions. Airborne observations can provide
61 very useful CCN measurements near cloud base but are expensive to collect and are limited to a
62 few field experiments, and having limited spatial-temporal coverage (Feingold et al., 1998; Li,
63 Liu, et al., 2015; Li, Yin, et al., 2015).

64 Overall, observations of CCN are spatiotemporally sparse, lack the vertical dimension, and provide
65 insufficient constraints on their global distribution. ACI studies often use satellite retrievals to take
66 advantage of their global coverage, but satellites have been unable to measure the CCN.
67 Nevertheless, the aerosol optical parameters such as aerosol optical depth (AOD) and aerosol index
68 (AI) are commonly used as proxies for CCN in previous studies (Gryspeerd & Stier, 2012; Patel
69 et al., 2017, 2019; Patel & Kumar, 2016; Quaas et al., 2008, 2009; Rosenfeld, 2008). However, all
70 these proxies are crude tools and suffer from various issues such as aerosol swelling, lack of
71 vertical information, cloud contamination, uncertainty in size distribution and solubility, and more
72 (Rosenfeld et al., 2016). The aforementioned studies based on passive satellite remote sensing
73 measurements, such as AOD and AI have limitations in several areas for ACI studies.

74 Active remote sensing technologies such as lidar have the ability to improve the precision and
75 range of conditions under which particle concentrations and their ability to act as CCN can be
76 retrieved. A significant body of prior studies has assessed the relationship between aerosol optical



77 properties and CCN based on local in situ data offered by lidar and radar. Feingold et al., (1998)
78 developed a technique to derive CCN from the retrieved cloud droplet concentration, vertical
79 velocity, and lidar backscatter from ground-based radar, lidar, and radiometer. Ghan et al., (2006)
80 and Ghan & Collins, (2004) evaluated the relationship between aerosol extinction from airborne
81 lidar and N_{CCN} from near-surface measurements and devised a technique for estimating CCN at a
82 cloud base. However, their techniques rely on the assumption that the physiochemical
83 characteristics of aerosols at the surface represent the vertical column. Thus, their retrievals may
84 be subject to large uncertainties due to vertical inhomogeneity in particle characteristics. Previous
85 work by Clarke & Kapustin, (2010); Kapustin et al., (2006); Liu & Li, (2014); Shinozuka et al.,
86 (2015) demonstrated a strong correlation between extinction coefficients and N_{CCN} instead of
87 vertically integrated AOD or AI using airborne and in situ observations. Stier, (2016) provided a
88 global assessment of the link between aerosol radiative properties and CCN using a global aerosol-
89 climate model (ECHAM-HAM) and suggested that vertically integrated aerosol radiative
90 properties are of limited suitability as a proxy for global surface CCN.

91 Both Mamouri and Ansmann, (2016) and Choudhury and Tesche, (2022) examine the potential of
92 single wavelength lidar observations to retrieve CCN number concentrations for different aerosol
93 types. The relationships between particle extinction coefficients and number concentrations of
94 particles with a dry radius larger than 50 nm (for non-dust) and 100 nm (for dust) were
95 parameterized based on multiyear AERONET observations for different aerosol types. However,
96 the measurements from the single wavelength lidar also lack sufficient information to quantify
97 particle size distribution, particle number concentration or aerosol type, resulting in large
98 uncertainty in N_{CCN} retrieval (Burton et al., 2012; Tan et al., 2019). However, few recent studies
99 (Lv et al., 2018; Tan et al., 2019) have shown efforts to retrieve N_{CCN} based on the advanced
100 capability of multiwavelength lidar measurements, but they have been limited to ground-based
101 observations only. Rosenfeld et al., (2016) have attempted a new approach to retrieve satellite
102 based N_{CCN} using passive satellite observations. All these studies taken together provide a sound
103 foundation of CCN-relevant aerosol properties, but most of them do not refer to CCN
104 concentrations themselves, and the ones who do, do not give a global coverage nor a vertically
105 resolved picture. Consequently, no reliable global observational data set of CCN exists, and the
106 ability to routinely measure vertically resolved CCN to study ACI effectively is still lacking
107 (Burkart et al., 2011).

108 In this study, we developed a comprehensive remote sensing algorithm with a novel retrieval
109 approach, known as ECLiAP (*Estimation of CCN using Lidar measured Aerosol optical*
110 *Properties*), to estimate N_{CCN} from multiwavelength spaceborne lidar measurements. The
111 approach is implemented with look-up table (LUT)s involving aerosol size and composition
112 information, in order to provide stable and efficient vertically-resolved CCN retrievals. The N_{CCN}
113 at six critical supersaturations ranging from 0.07%-1.0% is determined from the retrieved particle
114 size distributions. The retrieval accuracy is assessed using simulated lidar backscatter and
115 extinction coefficients with both random and systematic errors. The structure of this paper is as
116 follows: This section provides the importance and motivation for retrieving N_{CCN} . Section 2
117 discusses the inversion approach for retrieving N_{CCN} (particularly from satellite observations). The



118 numerical simulations for the sensitivity analysis, an extensive validation effort, and an
119 observational case study are presented in section 3. Section 4 covers the final discussion.

120 **2 Methodology**

121 **2.1 Construction of Lookup Tables**

122 The inversion solution using the combination of simultaneous measurements of backscatters at
123 three wavelengths and extinction at two wavelengths, also called $3\beta+2\alpha$, using lidar has been
124 gaining prominence for aerosol microphysical (effective radius, total number, volume
125 concentration, refractive index) retrieval (Burton et al., 2016). Several fundamental aspects of the
126 mathematical problem must be solved during the retrieval from multiwavelength lidar. The most
127 important aspect is that the inversion solution is not unique. The non-uniqueness of an inversion
128 solution in the advanced $3\beta+2\alpha$ technique is the primary source of the retrieval challenges
129 (Chemyakin et al., 2016). Additionally, retrieving six size parameters (number concentrations,
130 effective radius, and geometric standard deviation for fine and coarse mode particles) for a bimodal
131 particle size distribution (PSD) from five known quantities (β_{355} , β_{532} , β_{1064} , α_{355} , α_{532}) is still an
132 ill-posed inversion problem. Besides, the existing spaceborne lidar instrument (CALIOP onboard
133 CALIPSO) provides the measurements at only two wavelengths (532 nm & 1064 nm). Considering
134 all these constraints and partially compensating the non-uniqueness problem, we employed the
135 LUT approach with a fine step of bimodal particle size distributions (PSDs) to derive aerosol size
136 parameters. The parameterization of bimodal lognormal PSD is described in section 2.1.1. The
137 fundamental design of the LUTs framework for lidar measurements builds to test the aerosol
138 optical properties that we target for precise information.

139 In the present study, the LUTs are designed using the $3\beta+3\alpha$ (β_{355} , β_{532} , β_{1064} , α_{355} , α_{532} , α_{1064})
140 technique for the individual aerosol types. An additional input at a longer wavelength improves
141 the retrieval accuracy for coarse mode particles (Lv et al., 2018). These LUTs contain aerosol
142 optical properties such as backscatter coefficients at 355, 532, and 1064 nm (β_{355} , β_{532} , β_{1064}) and
143 extinction coefficients at 355, 532, and 1064 nm (α_{355} , α_{532} , α_{1064}), along with size parameters
144 including number concentration, effective radius and geometric standard deviation for fine and
145 coarse mode particles (N_{if} , r_f , σ_f , N_{ic} , r_c , σ_c). Primarily, the LUTs are generated for the five distinct
146 aerosols subtypes: marine, dust, polluted continental, clean continental, and smoke aerosols (as
147 shown in Figure 1). This study considers dust particles to be spheroid, while other aerosol types to
148 be spheres. The particle optical properties are computed using the well-known Mie scattering
149 theory (Bohren & Huffman, 1998) for spherical particles, which is a numerically accurate approach
150 over a wide range of particle sizes. Meanwhile, the T-Matrix method (Mishchenko & Travis, 1998)
151 is adopted for the spheroids, which is numerically precise for the limited particle sizes.
152 Consequently, the improved geometric optics method (IGOM; Bi et al., 2009; Yang et al., 2007)
153 is applied to the larger spheroids not covered by the T-matrix method. The axis ratio distribution
154 for spheroids, ranging from ~ 0.3 (flattened spheroids) to ~ 3.0 (elongated spheroids) is taken from
155 Dubovik et al., (2006). PSD and mean complex refractive index were used as the input parameters
156 for the computations of aerosol optical properties. The range of PSDs in the LUTs is sufficiently



157 broad to cover realistic values for atmospheric aerosols (Dubovik, 2002; Torres et al., 2017). The
158 parameters of bimodal distribution for five aerosol subtypes are derived using the measurements
159 from sun/sky radiometer at multiple selected Aerosol Robotic Network (AERONET) sites
160 (Dubovik, 2002; Torres et al., 2017). The PSDs are given in terms of the total particle number
161 concentration, effective radius (r), and geometric standard deviation individually for fine and
162 coarse modes. Table S1 lists the parameters of the bimodal lognormal PSDs and complex refractive
163 index that were used for the construction of LUTs. In the calculations, the range of radius for the
164 PSD is constrained to 0.01-10 μm with a fixed bin size of 0.002 defined on a logarithmic-
165 equidistant scale. The intervals of σ_f , σ_c , r_f and r_c are fixed at 0.01, 0.01, 0.002 and 0.01 μm ,
166 respectively. These intervals are set as a compromise between accuracy and computation time. The
167 parameterization of bimodal particle size distribution is discussed in the following section.

168 2.1.1 Lognormal Aerosol Size Distributions

169 An earlier study by Kolmogorov, (1941) mathematically proved that the random process of
170 sequential particle crushing leads to a lognormal distribution of particle size. In our study, PSDs
171 have been treated as a bimodal lognormal distribution, as widely used in aerosol remote sensing
172 studies (Dubovik et al., 2011; Remer et al., 2005; Schuster et al., 2006; Torres et al., 2014).
173 Although particle size distributions are not always bimodal in each case, their size distributions
174 can be considered as a combination of fine and coarse modes. This bimodal lognormal size
175 distribution can be expressed as:

$$\frac{dn(r)}{d \ln(r)} = \sum_{i=f,c} \frac{N_{ti}}{(2\pi)^{1/2} \ln \sigma_i} \exp \left[-\frac{(\ln r - \ln r_i^n)^2}{2(\ln \sigma_i)^2} \right] \quad (1)$$

176 where N_{ti} is the total particle concentration of the i^{th} mode and r_i^n is the median radius for the
177 aerosol size distribution, with n representing the number concentration distribution. The index $i =$
178 f, c refers to the fine and coarse modes, respectively. The term $\ln \sigma_i$ is the mode width of the i^{th}
179 mode. This general bimodal lognormal size distribution shape for aerosol is adopted in this study
180 to improve the accuracy of the CCN retrieval. The sensitivity assessment regarding the response
181 of CCN to the assumption of bimodal size distributions is presented in section 3.1. For individual
182 lognormal components, the relationships between the volume and number distribution parameters
183 representing by the following equations (Hatch & Choate, 1929):

$$r^n = r^v / \exp[3(\ln \sigma)^2] \quad (2)$$

$$V_t = N_t \frac{4\pi}{3} (r^n)^3 \exp \left[\frac{9}{2} (\ln \sigma)^2 \right] \quad (3)$$

184 where, V_t is the particle volume concentration and r^v is the median radius for the aerosol volume
185 size distribution. As shown in Figure 1 and Table S1, the main difference between the aerosol
186 subtype is the ratio of the volume concentration of the fine mode to the coarse mode.



187 2.2 Retrieval of CCN Number Concentrations

188 This section discusses a detailed methodology adopted by ECLiAP to retrieve N_{CCN} from
189 the given lidar measurements.

190 2.2.1 Overview

191 An optically related N_{CCN} is introduced to bridge the gap between aerosol particle and their
192 activation capability to serve as a cloud droplet. The ability of particles to act as CCN is mainly
193 controlled by particle size distribution followed by chemical composition (Dusek et al., 2006; Patel
194 & Jiang, 2021). However, both factors are significant in specific regions and meteorological
195 conditions (Mamouri & Ansmann, 2016). Therefore, N_{CCN} could be quantified with size
196 distribution and compositional information. The key feature of an approach adopted in ECLiAP is
197 to seek the parameters that can provide the size and composition of particles consistent with lidar
198 measurements under dry conditions and use these parameters to estimate N_{CCN} .

199 Figure 2 illustrates a schematic diagram of the method to retrieve N_{CCN} from satellite observations.

200 In the natural environment, the particle hygroscopic properties influence the particle size
201 distribution and their optical properties, especially when it is near a cloud base or under a high
202 moist environment. Therefore, the lidar measured aerosol optical properties under ambient
203 conditions need to be corrected to the dry aerosol optical properties using the hygroscopic
204 enhancement factor. The hygroscopic enhancement factor can be fitted by the parameterization
205 scheme using enhancement of backscatter and extinction coefficients with RH. Particle dry
206 backscatter and extinction can also be inferred from the hygroscopic enhancement factor. An
207 approach to computing hygroscopic enhancement factors and performing hygroscopic correction
208 to obtain dry backscatter and extinction is described in Section 2.2.2. This step is applied to all the
209 $3\beta+3\alpha$ parameters before looking for aerosol size parameters from the LUT. Before applying
210 hygroscopic correction, lidar-measured optical properties, particularly for dust mixtures, are
211 separated into dust and non-dust components using the backscatter coefficients and particle
212 depolarization ratio (Tesche et al., 2009). The methodology to separate the dust mixture is
213 discussed in Appendix A1.

214 Once the dry aerosol optical properties are derived, an ECLiAP look for the suitable size
215 parameters from the LUTs for the given dry aerosol optical properties and respective aerosol
216 subtype (see section 2.2.3). As mentioned earlier, the ability of particles to act as CCN is mainly
217 controlled by particle size distribution followed by chemical composition. Deriving composition
218 information of particles from the lidar measurements is not yet well-defined. Therefore, in the
219 absence of chemical composition data, mean chemical composition information denoted by a
220 single value of κ , the so-called hygroscopicity parameter, is achievable for estimating N_{CCN} , which
221 describes the relationship between the particle dry diameter and CCN activity. The sensitivity of
222 the estimated N_{CCN} to κ depends strongly on the variability of the shape of the aerosol size
223 distribution (Wang et al., 2018). Therefore, the chemical information becomes less important in



224 estimating N_{CCN} , especially at higher supersaturation (Patel & Jiang, 2021). Most studies reported
225 that the uncertainty of using the mean value of κ to estimate the N_{CCN} is less than 10% (Jurányi et
226 al., 2010; Wang et al., 2018), which varies with atmospheric conditions. In ECLiAP, the literature
227 values of κ are considered for each aerosol subtype for further retrieval. The κ is assumed to be
228 0.7 for marine (Andreae & Rosenfeld, 2008), 0.03 for dust (Koehler et al., 2009), 0.27 for polluted
229 continental (Liu et al., 2011), 0.3 for clean continental (Andreae & Rosenfeld, 2008), and 0.1 for
230 smoke aerosols (Petters et al., 2009) for the later computations.

231 Finally, an ECLiAP uses the retrieved optically equivalent size parameters from LUTs and κ value
232 as composition information for the further computation of critical radius using the κ -Köhler theory
233 (Petters & Kreidenweis, 2007), and hence the N_{CCN} for the six fixed supersaturations (see section
234 2.2.4). For the dust mixture, N_{CCN} derived separately both for dust and non-dust are added lastly.

235 2.2.2 Derivation of dry backscatter and dry extinction

236 It is difficult to measure the complex chemical composition and associated water uptake capability
237 of a particle with increasing RH. Therefore, a widely popular and simple parameterization scheme
238 was used to describe the changes in aerosol optical properties with atmospheric RH relative to a
239 dry (or low-RH) state, also called the hygroscopic enhancement factor. Recent aerosol hygroscopic
240 studies (Bedoya-Velásquez et al., 2018; Fernández et al., 2018; Lv et al., 2017) have derived
241 backscatter and extinction enhancement factors using lidar measurements and RH profiles. The
242 hygroscopic enhancement factor that is associated with both particle size and hygroscopicity
243 (Kuang et al., 2017), is defined as:

$$f_{\xi}(RH, \lambda) = \frac{\xi(RH, \lambda)}{\xi(RH_{dry}, \lambda)} \quad (4)$$

244 where f_{ξ} is the hygroscopic enhancement factor of the optical property ξ (backscatter and
245 extinction) at a specific light wavelength λ and RH, and RH_{dry} is the reference RH value (RH=0%).
246 There is no generic reference RH that represents the dry conditions for lidar measurements, unlike
247 in-situ controlled RH measurements, to derive enhancements factor. Inferring dry backscatter and
248 extinction coefficients is also crucial in CCN retrieval. Therefore, parameterization of the
249 hygroscopic growth of lidar-derived optical properties should combine dry aerosol optical
250 properties and $f_{\xi}(RH, \lambda)$ together. Previous studies have proposed several parameterization
251 schemes for hygroscopic enhancement factors (Titos et al., 2016). The most frequently used
252 parameterization scheme is a power-law function that is known as gamma parameterization,
253 introduced by Kasten, (1969):

$$f_{\xi}(RH, \lambda) = A \cdot (1 - RH/100)^{-\gamma} \quad (5)$$

254 Where the parameter A gives the extrapolated value at RH=0% and the exponent γ is the fitting
255 parameter and defines the hygroscopic behavior of the particles. Recently, a new physically based



256 single-parameter representation approach was proposed by Brock et al., (2016) to describe the
257 hygroscopic enhancement factor. Their results claimed that this proposed parameterization scheme
258 better describes light-scattering hygroscopic enhancement factors than the widely used gamma
259 power-law approximation. The formula of this new scheme is written as:

$$\xi(RH, \lambda) = \xi_{dry}(RH, \lambda) \cdot f_{\xi}(RH) = \xi_{dry}(RH, \lambda) \cdot \left[1 + \kappa_{\xi}(\lambda) \frac{RH}{100 - RH} \right] \quad (6)$$

260 where, κ_{ξ} is a dimensionless fitting parameter and shows a significant correlation with bulk
261 hygroscopic parameter κ ; but they are not equivalent (Brock et al., 2016; Kuang et al., 2017). ξ_{dry}
262 denotes dry aerosol optical properties (backscatter and extinction coefficients).

263 For the estimation of the hygroscopic enhancement factor, aerosol optical properties (backscatter and
264 extinction coefficients) at 355, 532, and 1064 nm are calculated over a range of RH (0-99%) using
265 Mie theory (T-matrix and IGOM for spheroid) for the range of PSDs and each aerosols subtype.
266 Figure S1 illustrates the mean curve of the hygroscopic enhancement factor (the ratio between the
267 aerosol optical properties at specific RH to dry RH) at three wavelengths with increasing RH for
268 each aerosol subtype. With given aerosol optical properties at different RHs, κ_{ξ} can be fitted by
269 curve fitting using Eq. (6). However, Tan et al., (2019), based on a comparison of κ_{ξ} and derived
270 ξ_{dry} for various ranges of RH, showed that the fitting hygroscopic parameters are found to be
271 sensitive to fitting RH range when the RH range is limited and relatively high (between 60% and
272 90%). Therefore, we fixed the RH range to 60%-90% for the parameter fitting (highlighted curve
273 in Figure S1). In addition, retrieving finite dry aerosol optical properties could not be possible for
274 the observation with RH > 99%. Therefore, ECLiAP only applies the hygroscopic correction when
275 RH is between 40% and 99%. In ECLiAP, individual κ_{ξ} values for each aerosol optical property
276 at three different wavelengths, along with the RH value, are used to obtain the dry aerosol optical
277 properties separately for each aerosol subtype using Eq. (6).

278 2.2.3 Inversion techniques for size parameters

279 Once the dry aerosol optical properties are obtained, the ECLiAP searches for suitable size
280 parameters from the LUTs. For this, the ECLiAP look for the best combination of six values (N_{if} ,
281 r_f , σ_f , N_{ic} , r_c , σ_c) to match inputs (β_{355} , β_{532} , β_{1064} , α_{355} , α_{532} , α_{1064}) by minimizing the following
282 function:

$$\mu^{sum} = \sum_{i=1, \dots, 6} \left| \frac{x_i - x'_i}{x_i} \right| \quad (7)$$

283 Where x_i represents input aerosol optical data (β_{355} , β_{532} , β_{1064} , α_{355} , α_{532} , α_{1064}) and x'_i is aerosol
284 optical data (β'_{355} , β'_{532} , β'_{1064} , α'_{355} , α'_{532} , α'_{1064}) derived from LUTs, which are calculated from
285 Mie theory (or T-matrix and IGOM for spheroid) and size distribution parameters.



286 Each LUT consists of two parts to reduce the dimensions and size of LUTs. Therefore, the particle
287 size distribution, as shown in Eq. (1), can be rewritten as:

$$\frac{dn(r)}{d \ln(r)} = \sum_{i=f,c} \left\{ \frac{1}{(2\pi)^{1/2} \ln \sigma_i} \exp \left[-\frac{(\ln r - \ln r_i^m)^2}{2(\ln \sigma_i)^2} \right] \cdot N_{ti} \right\} = \sum_{i=f,c} x_i \cdot N_{ti} \quad (8)$$

288 Where x_f and x_c refer to the data bank precomputed with $(\sigma_f, r_f$ and $r)$ and $(\sigma_c, r_c$ and $r)$,
289 respectively. Furthermore, we have adopted the successive approximation method (Kantorovitch,
290 1939) to deal with the extensive range of N_{tf} and speed up the finding for the closest solution.
291 Therefore, the inversion technique is further divided into two steps. Step-1: search for an
292 approximate solution based on the criterion in Eq. 8 and calculate the corresponding aerosol optical
293 data $(\beta'_{355}, \beta'_{532}, \beta'_{1064}, \alpha'_{355}, \alpha'_{532}, \alpha'_{1064})$ from the data banks $(x_f$ and $x_c)$ and N_{tf} and N_{tc} . The step
294 widths of N_{tf} and N_{tc} are considered to be 100 and 0.1 cm^{-3} , respectively. Step 2: based on the
295 approximate solution obtained in step 1, determine the smallest solution space of N_{tf} by repeating
296 the procedure in step 1 using a smaller step width of 10 cm^{-3} for N_{tf} . Search for the optimal solution
297 of six size parameters $(N_{if}, r_f, \sigma_f, N_{ic}, r_c, \sigma_c)$.

298 2.2.4 Estimation of N_{CCN}

299 For the given aerosol optical properties, the retrieved size parameters and the associated
300 hygroscopicity parameter (κ ; as discussed in section 2.2.1) were used to calculate the critical
301 radius. The critical radius (r_{crit}) above which all particles are activated into droplets for a certain
302 supersaturation ratio (S_c) can be computed from the κ -Köhler theory as suggested by Petters &
303 Kreidenweis, (2007):

$$D_{crit} = \left(\frac{4A^3}{27 * \kappa * \ln(S_c)^2} \right)^{1/3}; \quad A = \frac{4\sigma_{s/a}M_w}{RT\rho_w} \quad (9)$$

304 Where, D_{crit} is the critical diameter ($r_{crit} = D_{crit}/2$), and $S_c = SS + 1$, M_w and ρ_w are the
305 molecular weight and water density, while R and T are the ideal gas constant and the absolute
306 temperature, respectively and $\sigma_{s/a} = 0.072 \text{ J m}^{-2}$. The critical radius is determined at six critical
307 supersaturations for activation (0.07%, 0.1%, 0.2%, 0.4%, 0.8% and 1.0%).

308 Finally, the ECLiAP calculates N_{CCN} by integrating size distribution from critical radius to
309 maximum radius as:

$$N_{ccn} = \int_{\ln r_c}^{\ln r_{max}} \frac{dn(r)}{d \ln(r)} d \ln(r) \quad (10)$$

310



311 3 Results

312 3.1 Sensitivity analysis

313 Evaluating the algorithm is a challenging task in the absence of standard and reliable
314 measurements. The performance of the ECLiAP is evaluated using numerically simulated
315 observations with different error characteristics.

316 3.1.1 Retrieval of N_{CCN} with error-free data

317 Firstly, error-free lidar measurements are considered as inputs to evaluate the inversion stability
318 of ECLiAP. The retrieval procedure is repeated for 2000 different sets of the bimodal size
319 distribution for each aerosol type. Errors are calculated in retrieved N_{CCN} (N_{CCN}^{ret}) with respect to
320 the initial inputs (N_{CCN}^{int}) using Eq. 8.

$$CCN\ Error = [(N_{CCN}^{ret} - N_{CCN}^{int})/N_{CCN}^{int}] \times 100\% \quad (11)$$

321 Table 1 lists the statistical results of CCN error for each aerosol type. As the number shows, the
322 initial N_{CCN} is well reproduced from the error-free inputs for each aerosol size distribution. The
323 standard deviation of the retrieved CCN errors from the different sets of bimodal size distribution
324 data is also estimated along with the mean value to determine the range of the retrieved CCN error.
325 As mentioned above, the appropriate balance between the accuracy and processing time of the
326 LUTs leads the mean CCN error close to zero but not equal to zero. However, the small standard
327 deviation (<0.25) indicates the smaller variances of errors among the aerosol size distributions.
328 Although the high accuracy of LUTs provides the CCN error closer to zero, the calculations are
329 more time expensive. In general, the retrieval results shown in Table 1 exhibit the good accuracy
330 and stability of the inversion algorithm for each aerosol subtype.

331 Additionally, the sensitivity of the N_{CCN} retrieval to the assumption of the bimodal size distribution
332 is tested against the aerosol size distribution measurements at the U.S Department of Energy's
333 Atmospheric Radiation Measurement (ARM) climate research facility from the Southern Great
334 Plain (SGP) site. Particle size distribution was measured simultaneously by an Ultra-High
335 Sensitivity Aerosol Spectrometer (for the 0.07 to 1 μm geometric diameter range) and an
336 Aerodynamic Particle Sizer (TSI-3321; for the 0.7 to 5 μm aerodynamics diameter range). The
337 size conversion factor, defined as the ratio of aerodynamic diameter to geometric diameter, was
338 used to construct a trimodal lognormal particle size distribution. For the purpose of this study, the
339 corresponding bimodal fits are produced, which are representative of the observed size
340 distributions. Figure S2 shows an example of the observed aerosol size distribution and the
341 corresponding bimodal fits. The comparison suggests that bimodal lognormal size distributions
342 can well represent the observed aerosol size distributions qualitatively. Later, we calculate N_{CCN}
343 based on the bimodal fits and compare them with the 100 observed size distributions to quantify
344 the errors arising from the bimodal lognormal fits. The associated κ values are estimated based on



345 observed PSDs and N_{CCN} values as described in Patel & Jiang, (2021). The induced CCN errors
346 from the bimodal fitting are shown in Table 2. The absolute value of N_{CCN} retrieval errors is 3.9%,
347 with a standard deviation of 2.8% at 0.1% supersaturation. Overall, the results suggest that bimodal
348 lognormal aerosol size distributions are adequate for retrieving N_{CCN} , but errors from the bimodal
349 assumption are not negligible.

350 3.1.2 Impact of systematic and random errors on N_{CCN} retrieval

351 Both systematic and random errors exist in lidar-retrieved measurements (Mattis et al., 2016).
352 Systematic errors can be induced by experimental conditions, retrieval algorithms, data processing
353 methods, and our understanding of physical interactions. Sensitivity analysis tests the impacts of
354 systematic errors from backscatter and extinction coefficients on N_{CCN} retrieval. Although the
355 systematic errors of different parameters are correlated, the errors are considered independent for
356 individual lidar measurements in the simulations. The systematic errors ranging from -20% to 20%
357 with an interval of 5% are applied to one input parameter at a time (others are kept error-free) in
358 each test to understand the impacts on individual parameters better. The inversion algorithm is
359 performed to obtain a new set of aerosol size distributions and retrieve N_{CCN} data. The procedure
360 is repeated for each input parameter and error value with 200 sets of the randomly generated size
361 distribution for each aerosol subtype. The percentage errors in N_{CCN} associated with systematic
362 errors can be estimated by comparing retrieved and initial values of N_{CCN} using Eq. 11.

363 Figure 3 illustrates the error in retrieved N_{CCN} as a function of the systematic errors in backscatter
364 and extinction coefficients. The slope of the curve indicates the sensitivity of CCN errors to
365 systematic errors in individual parameters. A steeper slope infers a high sensitivity in the N_{CCN}
366 retrieval to the systematic error for a given input parameter. Errors in retrieved N_{CCN} increase as
367 errors of backscatter and extinction increase, and it is even steeper at higher supersaturations. In
368 general, N_{CCN} retrievals are most sensitive to errors in extinction coefficients followed by
369 backscatter coefficients. Interestingly, the results are less sensitive to errors in backscatter
370 coefficients at lower supersaturations ($\leq 0.2\%$) but are relatively more sensitive at higher
371 supersaturations ($> 0.2\%$). This indicates that reducing uncertainties in the extinction coefficients
372 can effectively improve the accuracy of N_{CCN} retrieval while reducing uncertainty in backscatter
373 coefficients can be beneficial for retrieving N_{CCN} at higher supersaturation. Errors in α_{355}
374 influence the retrieval results the most. On average, a positive relative error of 20% in α_{355}
375 overestimates the N_{CCN} retrieval by about 20% at lower supersaturation and about 50% at higher
376 supersaturation. A negative error of 20% in α_{355} underestimates the N_{CCN} retrieval, and the degree
377 of impact is slightly higher than the positive error. Errors in α_{532} and α_{355} have the opposite effect
378 on the retrieval error. It is also clear that the influence of systematic errors on the retrieval of N_{CCN}
379 varies with activation radius, as elucidated by the different signs of the slopes. For instance, the
380 slopes of the extinction coefficient for dust aerosols reverse the sign when the activation radius
381 exceeds low to high supersaturation. These differences most likely result from the reduced retrieval
382 sensitivity to the coarse mode of the aerosol size distribution. In addition, there are substantial
383 distinctions among the types of aerosols. Dust and marine aerosols have the largest absolute errors



384 compared to others dominated by fine-mode particles (see Table 1). These collectively indicate
385 that there are better constraints for fine-mode aerosols than for coarse-mode aerosols, which
386 introduce a larger retrieval error in N_{CCN} for aerosols with more weight in the coarse mode. It is
387 noteworthy that incorporating an additional input signal of extinction coefficient at 1064 nm in the
388 ECLiAP reduces the error by $\sim 20\%$ in the coarse mode-dominated aerosol subtypes (dust and
389 marine), and $\sim 15\%$ in total compared to the previous studies (Lv et al., 2018; Tan et al., 2019).
390 Nevertheless, integrating an additional lidar signal at a wavelength longer than 1064 nm may
391 further reduce retrieval error for the coarse mode-dominated aerosol type.

392 RH is another crucial parameter in the present retrieval algorithm for N_{CCN} . Errors in RH derived
393 by remote-sensing or reanalysis influence the values of growth factors and result in the dry aerosol
394 optical properties, which in turn influence all the input parameters. Therefore, systematic errors
395 ranging from -10% to 10% in intervals of 2% are considered for RH. Figure 4 shows the result of
396 systematic errors in RH. We observed that N_{CCN} is overestimated when RH has a negative
397 systematic error, and the extent of overestimation in N_{CCN} increases as the error increase. A
398 negative error of 10% in RH overestimates N_{CCN} at lower supersaturation by about 20% and
399 doubles at higher supersaturation. The effects of the positive errors in RH are relatively smaller
400 and more complicated than negative errors. The mean retrieval error peaked at the RH error at 6% ,
401 and the standard deviation of retrieval error increased with the RH error. This suggests that
402 underestimating RH causes large errors than overestimation. Therefore, extra care should be paid
403 to RH measurements if RH-related hygroscopic enhancements of aerosol optical properties are
404 considered.

405 Systematic errors introduce mean biases in N_{CCN} retrievals, whereas random errors in observations
406 produce random N_{CCN} retrieval errors. Random errors obeying Gaussian distributions are produced
407 arbitrarily with a mean value of zero. The standard deviations are set to 10% for aerosol optical
408 properties and to 5% , 10% , and 20% for RH in each test. The simulation is repeated 5000 times
409 for each aerosol subtype, and the statistical results are presented in Figure 5. The mean values of
410 relative error are presented by color, and the number indicates the standard deviation. The error
411 does not change significantly as the random error of RH increases. The mean random errors are
412 relatively small and non-zero, mainly because the sensitivities of N_{CCN} retrievals are different for
413 different aerosol optical data. The standard deviations are within 16% - 28% . The results reveal that
414 random errors in the given input parameters may also contribute to systematic errors in the N_{CCN}
415 retrievals. The largest mean relative errors are found for coarse mode-dominated aerosol subtypes
416 (dust and marine), consistent with the sensitivities to systematic errors. As discussed earlier,
417 considering additional lidar measurements at longer wavelengths that are more sensitive to larger
418 particles could improve the retrieval of N_{CCN} for the coarse mode-dominated aerosol subtypes. The
419 mean values of relative errors increase with increasing supersaturation for all aerosol types. Errors
420 in the retrieved N_{CCN} follow a Gaussian distribution for low supersaturation. However, the
421 Gaussian shape disappears, and the high frequencies shift to the edge of the distribution when
422 supersaturation shifts from low to high (not shown here). Furthermore, the influence of random
423 errors on the individual input parameters is also assessed and is shown in Figure S3. Random errors



424 underestimate the enhancement factor (κ_{ξ}) by 30%-40% for 5% RH error, 45%-60% for 10% RH
425 error, and 65%-75% for 20% RH error. The relative errors in β are likely to be overestimated,
426 whereas they are underestimated in α . The absolute relative error of input parameters becomes
427 larger as the random error of RH grows.

428 3.2 Comparison with airborne measurements

429 The evaluation of N_{CCN} retrieval depends on how well retrieved and observed values are matched,
430 as matching errors can become overwhelming. Therefore, we have carried out a validation
431 approach by comparing ECLiAP retrieved N_{CCN} from lidar measurements with the in-situ
432 measurements of N_{CCN} by CCN counter during the NASA ObseRvations of Aerosols above Clouds
433 and their intEractionS (ORACLES) airborne campaign, which occurred from 2016 to 2018 over
434 the Southeast Atlantic (SEA) (Redemann et al., 2021; Zuidema et al., 2016). The ORACLES data
435 contain measured in-situ N_{CCN} from the CCN counter and lidar measurements with NASA Langley
436 Research Center's high-spectral resolution lidar (HSRL-2). We took the opportunity to conduct
437 the validation exercise based on the accessible data.

438 HSRL-2 measures the vertical profiles of aerosol optical properties, whereas the CCN counter
439 provides measurements for point location. Therefore, we carried out two strategically different
440 validation exercises in this study: (1) the vertical profile-based comparison and (2) the comparison
441 of collocated measurements. For the profile-based comparison, an ascending path of flight (area
442 covered within the yellow dashed line in Figure S4) on 19 October 2018 has been considered, so
443 the measurements of the CCN counter can be available at various altitudes. Prior to comparison,
444 the lidar measurements from HSRL-2 are averaged over a selected wide space and time (yellow
445 dashed line box in Figure S4). The N_{CCN} measurements from the CCN counter were available at
446 the supersaturation between 0.32% and 0.34%. Hence, the N_{CCN} were retrieved at the
447 supersaturation of 0.34% by applying ECLiAP to the mean profiles of lidar measurements. It is
448 noteworthy that the retrieval has been carried out only on those observations having valid lidar
449 measurements at least for two wavelengths. Figure 6a demonstrates the retrieval fit to HSRL-2's
450 vertical dry aerosol extinction coefficient measurements at 355, 532, and 1064 nm. A smoke
451 aerosol dominates the ~93% of profiles at the altitude above 800 meters and marine at lower
452 altitudes (< 800 m), having RH between 30%-105%. The finite dry aerosol optical properties close
453 to the surface could not be retrieved for the observations with RH>99%. The retrieved profiles of
454 dry extinction coefficients are in better agreement with the measured by HSRL-2. This illustrates
455 the ability of the kappa parametrization to account for aerosol hygroscopicity. The vertical mean
456 of absolute fitting error of extinction coefficient is found to be 3.2%, 4.8%, and 6.3% for 355, 532,
457 and 1064 nm, respectively, and the vertical mean of absolute fitting error of backscatter
458 coefficients is 5.1%, 6.7% and 8.9% for 355, 532 and 1064 nm respectively. The fit to the
459 backscatter coefficients of 1064 nm has a relatively larger error. Certainly, one needs to know that
460 the vertically resolved extinction coefficient at 1064 nm is derived using the backscatter coefficient
461 at 1064 nm and lidar ratio. Since HSRL-2 does not directly measure extinction at 1064 nm, it is
462 computed from an assumed relationship with the measured lidar ratio at 532 nm. Though provided



463 as a best guess, such an estimate may cause extra uncertainty to the 1064 nm. Furthermore, the
464 comparison of vertical profiles of ECLiAP retrieved N_{CCN} from lidar measurements and the N_{CCN}
465 measured by the CCN counter is shown in Figure 6b. The retrieved values captured the pattern of
466 altitude variations in N_{CCN} as observed by the in-situ measurements. However, the magnitude of
467 retrieved N_{CCN} is slightly overestimated by $\sim 12\%$ in total. The overestimation is lower ($\sim 9\%$) at
468 above 2 km, whereas, at below 1 km, it is slightly higher ($\sim 16\%$). A plausible reason behind the
469 relatively large overestimation at below 1 km might be the considerable variation of RH between
470 60%-105% or/and the highly variable aerosol properties due to the mixture of multiple aerosol
471 subtypes (smoke, marine, and dust). In addition, wind-driven advection and the age of the air parcel
472 radically modify the characteristics of smoke aerosols and their hygroscopic behavior, which also
473 leads to the slight overestimation of retrieved N_{CCN} values. The discrepancy between the retrieved
474 and observed values of N_{CCN} should be reassessed with the robust measurements from the varieties
475 of aerosol subtypes using the multi-campaign airborne data.

476 The second robust validation exercise is performed, based on collocated measurements,
477 using two years (2017-2018) of combined data from the ORACLES campaign. In 2017-2018, both
478 HSRL-2 and CCN counter were installed on the NASA P-3 flight. The end goal of this exercise is
479 to find one lidar measurement from HSRL-2 to directly compare with one N_{CCN} measured by the
480 CCN counter, both observed in approximately the same time and space. We defined collocation
481 criteria for any given HSRL-2 profile as follows. The collocation method finds CCN measurement
482 that falls within ± 1.1 km horizontal distance, ± 60 m vertical distance, and ± 10 minutes of the time
483 window. Later, the meteorological parameters within the given space and time windows are
484 extracted along with lidar measurements and measured N_{CCN} from each flight of the 2017-2018
485 ORACLES campaign. ECLiAP is applied to each lidar measurement for N_{CCN} retrieval on the
486 same supersaturation value measured by the CCN counter (lies within the range from 0.2-0.4%
487 SS). Figure 7 represents the result from the comparison of retrieved and measured N_{CCN} . The N_{CCN}
488 inferred from the CCN counter measurement is in better agreement with the retrieved N_{CCN} with a
489 correlation coefficient (R) of ~ 0.89 , a root mean square error (RMSE) value of 302.8 cm^{-3} , and a
490 bias of 138.8 cm^{-3} . The systematic positive bias in the comparison indicates that the retrieved N_{CCN}
491 are overestimating the observed values. It is noteworthy that smoke aerosols dominate in the
492 observations from ORACLES, but it also has significant observations from marine, dust, and
493 polluted dust. The discrepancy between measured and retrieved values could be due to the
494 variabilities in the aerosol properties. Overall, the strong correlation in the validation results
495 demonstrates the potential of ECLiAP in retrieving N_{CCN} from lidar measurements. It recommends
496 having a detailed validation study separate for aerosol subtypes using ground-based and aircraft
497 measurements to evaluate the reliability of the ECLiAP algorithm in estimating the N_{CCN} .

498 3.3 Retrieving N_{CCN} from spaceborne lidar (CALIOP/CALIPSO): a case study

499 Extending the scope of ECLiAP, the methodology was converted into a procedure that can be
500 applied to any level-2 aerosol profile dataset from Cloud-Aerosol Lidar with Orthogonal
501 Polarization (CALIOP) on the Cloud-Aerosol Lidar and Infrared Pathfinder Satellite Observations



502 (CALIPSO) (Winker et al., 2007). As an illustrative example, this procedure was applied to a
503 regular CALIPSO track for 01 January 2019 starting at 20:08 UTC, which spans from 10 °N to 40
504 °N, passing over the Tibetan plateau and Indian landmass. The CALIPSO track (solid black line)
505 can be seen on the right-hand side in Figure 8a. CALIOP onboard CALIPSO provides
506 measurements of aerosol optical properties only at two wavelengths (532 and 1064 nm). Therefore,
507 a total of six parameters (β_{532} , β_{1064} , α_{532} , α_{1064} , *depolarization ratio*, and *aerosol subtypes*) from
508 CALIOP along with meteorological parameters (RH, temperature) are provided as the inputs to
509 ECLiAP and retrieved total particle concentration (N_{CN}) and N_{CCN} at six supersaturations as
510 outputs. The N_{CN} amount represents the total number of aerosol particles that can serve as centers
511 for condensation, while the N_{CCN} is the fraction of N_{CN} that can activate as CCN.

512 The extinction coefficient at 532 nm and aerosol subtypes, along with retrieved N_{CN} and N_{CCN} at
513 supersaturation of 0.4%, are shown in Figure 8. Unfortunately, due to the retrieval limitation over
514 the elevated region along with cloudiness, there are no valid aerosol measurements over the
515 Himalayan-Tibetan plateau (as shown by a gap between 28 °N to 37 °N). On the contrary, a strong
516 mixed aerosol signal is observed over the Indian landmass (α_{532} larger than 2.5 km⁻¹), while an
517 elevated (altitude >1 km) dust aerosol layer (α_{532} = ~1.0 km⁻¹) at the edge of the CALIPSO track
518 over the Taklamakan desert (above 38 °N). Over southern India (below 17 °N), polluted
519 continental aerosols prevail (α_{532} between 0.5-0.8 km⁻¹) and mostly accumulate within the
520 boundary layer (~1.5 km a.s.l.), while over northern India (above 19 °N), the aerosol situation
521 includes a mixture of polluted continental and polluted dust (α_{532} = ~1.6 km⁻¹ below 1 km altitude).
522 The corresponding vertical cross-section of retrieved N_{CN} and N_{CCN} at a supersaturation of 0.4%
523 using ECLiAP can be seen in Figures 8c and 8d, respectively. N_{CN} and N_{CCN} larger than 25000
524 cm⁻³ and 3000 cm⁻³ at a supersaturation of 0.4% appear over the areas where polluted continental
525 aerosols dominate (southern India), while N_{CCN} is greater than 2000 cm⁻³ appears over northern
526 India. Dust N_{CCN} of 100 to 200 cm⁻³ appears over the Taklamakan desert region.

527 To verify the capability of ECLiAP retrieval to capture similar variability of particle
528 physicochemical characteristics and its influence on CCN retrievals, we have investigated two
529 distinct cases identified based on the variation in aerosol subtypes and meteorological variables.
530 These scenarios are as follows: (1) Case-I: domination of polluted continental aerosols over
531 southern India (red color box covered in figure 8) (2) Case-II: Mixture of polluted dust and polluted
532 continental aerosols over northern India (blue color box covered in figure 8). The profiles of
533 extinction coefficients at 532 nm and relative humidity, along with retrieved N_{CN} and N_{CCN} at six
534 supersaturations, are presented in Figure 9. Figure 9a shows the profiles of the extinction
535 coefficient at 532 nm and relative humidity for both cases. The extinction profile in case-I ranges
536 from 0.7-1.2 km⁻¹, is dominated by polluted continental aerosols in the high moisture condition
537 (RH between 60%-80%), accumulates within the boundary layer (~1.5 km), and peaks at ~1.2 km.
538 Conversely, case-II represents the low moisture condition (RH ≤ 30%), with relatively large
539 extinction coefficient values with a maximum of 1.6 km⁻¹ at ~0.2 km altitude, influenced mainly
540 by the mixture of polluted continental and polluted dust aerosols. These two cases are dynamically
541 diverse and different in nature that providing a solid platform to verify the capability of ECLiAP



542 in retrieving N_{CCN} . Figure 9b illustrates the retrieved N_{CN} using ECLiAP for both cases. The
543 retrieved mean values of N_{CN} are observed to be almost similar ($\sim 12000\text{ cm}^{-3}$ and $\sim 11000\text{ cm}^{-3}$ for
544 case-I and case-II, respectively). The profiles of N_{CN} follow a similar vertical distribution pattern
545 of extinction coefficients. Figures 9c and 9d display the retrieved N_{CCN} at six supersaturations for
546 Case-I and II, respectively. Interestingly, N_{CCN} values are found to be relatively lower in case-II,
547 though its extinction coefficient is larger than in case-I. Note that ECLiAP considers polluted dust
548 as a mixture of polluted continental and dust aerosol to retrieve N_{CCN} . The above-mentioned
549 discrepancy can be only explained by the intrusion of dust and its non-hygroscopic behavior along
550 with dry conditions, further reducing the concentration of hygroscopic aerosols that leads to a
551 decrease in N_{CCN} . This has been clearly reflected in the calculated activation ratio ($AR =$
552 N_{CCN}/N_{CN}) spectra in Figure S5. Figure S5 directly compares the AR spectra as a function of SS
553 for both cases. The observed differences in the AR spectra reflect the nature of the particles to act
554 as CCN. Relatively, larger values of AR in case-I indicate the dominance of hygroscopic aerosols
555 get activated to CCN under high moisture and increase N_{CCN} . In contrast, the dust intrusion in
556 case-II reduces the capability of particles to activate as CCN under low moisture and further
557 reduces AR by $\sim 20\%$ – 60% for the range of supersaturation from 0.07% to 1.0%. Given the limited
558 sample space, the aim of the study is to demonstrate the potential of ECLiAP for retrieving reliable
559 N_{CCN} data from spaceborne lidar measurements. A detailed comprehensive analysis comparing the
560 CALIOP-retrieved N_{CCN} with multi-campaign airborne measurements is essential to evaluate the
561 reliability of ECLiAP to construct the 3D CCN climatology at a global scale.

562 4 Discussion

563 Due to the absence of vertically resolved information in AOD, using it as a proxy for CCN in ACI
564 studies has several shortcomings. Among other issues, a column property like AOD is not
565 necessarily representative of N_{CCN} at altitudes, which affects the formation and growth of the cloud.
566 Because no reliable global estimate of N_{CCN} exists, the fundamental assumptions of ACI cannot
567 be robustly verified with the available sparse and localized in-situ measurements. In this study, we
568 present a novel approach based on the $3\beta+3\alpha$ technique for retrieving vertically-resolved cloud-
569 relevant N_{CCN} from a single spaceborne lidar sensor. With this development, we demonstrate a
570 new application of active satellite remote sensing that can provide direct measurements of CCN to
571 improve understanding of ACI processes.

572 To address the problem of the non-uniqueness of a solution in the $3\beta+2\alpha$ inverse technique, we
573 have adopted a more realistic LUT-based approach using the $3\beta+3\alpha$ multiwavelength technique,
574 reflecting the bimodal particle distribution in the atmosphere better. Previous studies (Lv et al.,
575 2018; Tan et al., 2019) demonstrated that CCN estimation is highly sensitive to the extinction
576 coefficient than the backscatter coefficient. Therefore, we have included an additional signal of
577 extinction coefficient at 1064 nm to improve the retrieval accuracy of particle size distribution,
578 particularly for coarse mode. In order to verify the performance, the CCN estimation error, using
579 Eq. 12, has been calculated using both $3\beta+2\alpha$ and $3\beta+3\alpha$ techniques for each aerosol subtype in
580 comparison to the observed CCN values. The relative difference in CCN estimation error between



581 $3\beta+2\alpha$ and $3\beta+3\alpha$ techniques for each aerosol subtype is shown in Figure 10. The analysis shows
582 that insertion of the α_{1064} signal in the $3\beta+3\alpha$ technique improves the CCN estimation by $\sim 15\%$ in
583 total and $\sim 20\%$ for the coarse mode dominated aerosol subtypes (i.e., marine and dust aerosols)
584 compared to $3\beta+2\alpha$. Based on CCN closure analysis, Patel & Jiang, (2021) suggested that particle
585 size and chemical composition are more crucial in the CCN activity at lower SS. In contrast, at
586 higher SS, most particles become activated regardless of their size and composition. Therefore,
587 the improvement in CCN estimation is relatively large in low SS ($SS < 0.2\%$) than in high SS (SS
588 $> 0.2\%$).

589 Systematic and random errors in the lidar measurements were evaluated individually and discussed
590 in the sensitivity analysis. Both systematic and random errors realistically coexist in optical
591 parameters, and therefore, we have evaluated their concurrent effect. The simulations were
592 conducted with both systematic and random errors co-occurring. The results (not shown here)
593 show that the retrieved CCN errors are much smaller than the error obtained individually by either
594 systematic or random at each wavelength independently. The mean CCN error ranges between
595 7%-15% at SS from 0.07% to 1.0%. This retrieved CCN error is slightly large ($\sim 12\%$ -18%) for
596 the coarse-mode dominated aerosol subtypes (dust and marine). Summing up errors from multiple
597 optical parameters might compensate for each other and improve the CCN retrievals. Furthermore,
598 the retrieval from ECLiAP has few constraints. (i) it strongly depends on the accuracy of lidar-
599 measured aerosol optical properties. The retrieval is only possible if the lidar signals are available
600 at least at two wavelengths. (ii) retrieval from ECLiAP is only performed for $RH \leq 99\%$. (iii) the
601 CCN activity also depends on the mixing state, which is difficult to measure from space.
602 Subsequently, an alternative solution is required to parametrize the effect of the mixing state on
603 CCN activity.

604 The present study demonstrates the capability of ECLiAP to construct the three-dimensional global
605 climatology of N_{CCN} . The global coverage of N_{CCN} , in conjunction with collocated retrieved cloud
606 properties, will provide crucial input for the regional and global simulations that will provide
607 realistic assessments of aerosol-induced cloud radiative forcing. The satellite-retrieved N_{CCN} can
608 precisely separate the aerosols into natural and anthropogenic components, which can be further
609 used for constraining aerosol emissions and transport models for air-quality studies. The
610 application of detailed N_{CCN} will potentially mitigate the uncertainty of aerosol perturbed climate
611 forcing (direct + indirect) and improve confidence in assessing anthropogenic contributions and
612 climate change projections.

613 5 Summary

614 CCN number concentration is a critically-important parameter to constrain the relationship
615 between aerosols and clouds and is needed to improve the understanding of ACI processes. The
616 lack of direct measurements of CCN prevents robust testing of the underlying assumptions
617 associated with aerosol-cloud interactions robustly and evaluates climate model simulations. In
618 order to overcome this limitation, we presented ECLiAP, an emergent remote sensing-based



619 analytical algorithm based on the physical law to retrieve the vertically resolved N_{CCN} from aerosol
620 optical properties measured by the multiwavelength lidar system. Among the several fundamental
621 aspects of the mathematical problem that must be solved during retrievals of microphysical
622 parameters from multiwavelength lidar, the most crucial aspect is that the inverse solution is not
623 unique. Therefore, the retrieval is implemented based on look-up tables generated from Mie
624 scattering (and T-matrix/IGOM for dust particles) calculations. AERONET-based five
625 representative aerosol subtypes with bimodal size distributions were considered. The influence of
626 relative humidity on lidar-measured aerosol optical properties is corrected using the aerosol type-
627 dependent hygroscopic growth factor to obtain the dry aerosol optical properties. As a tradeoff
628 between the accuracy and computation time of the inversion, a successive approximation technique
629 is utilized in two steps to retrieve the optically equivalent particle number size distribution. Once
630 the aerosol size distribution parameters are obtained through the LUT, critical diameter and N_{CCN}
631 at six supersaturations ranging from 0.07% to 1.0% is estimated using the κ -Köhler theory.

632 Sensitivity analyses were carried out to evaluate the algorithm performance and to show the
633 influence of systematic and random errors of lidar-derived optical properties and auxiliary RH
634 profiles on CCN retrieval. The performance of ECLiAP is evaluated with error-free data, and N_{CCN}
635 at all six supersaturations is well reproduced with good accuracy and stability for the five aerosol
636 subtypes. Systematic errors in extinction coefficients and RH greatly influence CCN retrieval
637 errors. Reducing uncertainties in extinction coefficients effectively improves retrieval accuracy,
638 while uncertainties in backscatter coefficients benefit retrieval at higher SS. Differences in weights
639 of fine- to coarse-mode particles within the aerosol subtypes lead to significant differences in the
640 retrieval uncertainty. The differences can be explained via the weaker constraint of the algorithm
641 for the coarse mode particles than for the fine mode. However, the insertion of the additional signal
642 at a relatively longer wavelength reduced the differences in the retrieval uncertainty compared to
643 previous techniques. The mean random errors are relatively small and found to be relatively large
644 for the coarse mode-dominated aerosol subtypes, consistent with the sensitivities to the systematic
645 errors. In realistic cases, systematic and random errors often offset each other and improve the
646 mean CCN retrievals. Overall, the error analysis suggests that extinction coefficients at 355 and
647 532 nm must be reliably derived to ensure retrieval accuracy, including measurements at longer
648 wavelengths further improve the CCN retrievals, particularly for the coarse mode-dominated
649 aerosol subtypes.

650 The ECLiAP algorithm was applied to observational data from the NASA ORACLES airborne
651 campaign to illustrate the potential of the algorithm. N_{CCN} retrieved from lidar (HSRL-2)
652 measurements have been validated against the simultaneous measurements from the CCN counter
653 installed in the flight. Considering the inhomogeneity in the vertical distribution of aerosols
654 throughout the atmospheric column, N_{CCN} from in situ measurements and lidar retrievals agree
655 well. Furthermore, for the first time, the ECLiAP has been applied to spaceborne lidar
656 measurements – CALIOP/CALIPSO – to retrieve N_{CCN} . The results demonstrate that the N_{CCN}
657 retrieved by ECLiAP is highly influenced by the variability of aerosol particle size and
658 composition based on aerosol subtypes and also captures the meteorological influence. The



659 vertically resolved information of aerosols, along with CCN from spaceborne lidar, is essential for
660 investigating the ACI in detail.

661 Our future goals include a comprehensive evaluation of N_{CCN} derived from spaceborne lidar
662 measurements, i.e., CALIOP/CALIPSO, with multi-campaign airborne measurements, covering
663 various physicochemical regimes in the troposphere. The extensive validation will enable us to
664 test the applicability of the ECLiAP algorithm in the context of estimating the N_{CCN} from space.
665 Eventually, we plan to apply the ECLiAP algorithm over the period of CALIOP observations (~15
666 years) to generate the global three-dimensional N_{CCN} climatology. The data set coupled with the
667 cloud-related data from the other satellite or state-of-the-art numerical models will help improve
668 our understanding of the ACI. The science narrative of the NASA Aerosol and Cloud, Convection
669 and Precipitation (ACCP) project pointed out that the combination of near-simultaneous and
670 collocated lidar and polarimeter measurements can provide more detailed information regarding
671 particle size, concentration, and composition (Braun et al., 2022). Therefore, our future work may
672 also include combining the lidar measurements with passive observations in the ECLiAP algorithm
673 to further narrow down the uncertainty of aerosol microphysics with the enhanced observational
674 constraints (Xu et al., 2021), which will in turn improve the accuracy of CCN retrieval. Moreover,
675 the ability of CALIOP to detect the aerosol subtypes has facilitated the retrieval of aerosol type-
676 specific 3D N_{CCN} climatology on a global scale. These datasets from spaceborne lidar
677 measurements will be beneficial for evaluating models and other satellite products, opening a new
678 window to investigate the region and regime-wise detailed ACI studies and better constraining
679 anthropogenic contributions to the climate forcing in the climate model.



680 **Appendix A1: Separation of optical properties for dust mixture**

681 We have adopted the methodology by Tesche et al., (2009) to separate the dust and non-
682 dust extinction coefficients in the dust mixtures (polluted dust and dusty marine) using particle
683 backscatter coefficients and particle depolarization ratio. The optical properties

$$\beta_d = \beta_p \frac{(\delta_p - \delta_2)(1 + \delta_1)}{(\delta_1 - \delta_2)(1 + \delta_p)} \quad (A1.1)$$

684 Where the values of δ_1 and δ_2 are 0.31 and 0.05, respectively. If $\delta_p > 0.31$ (< 0.05) then aerosol
685 mixture has considered to be pure dust (non-dust). For the remaining values of δ_p , we first estimate
686 β_d using the above equation and then calculate β_{nd} by subtracting β_d from β_p . Later, the extinction
687 coefficients are computed by multiplying the backscatter coefficients with the respective lidar ratio
688 (44, 70, and 23 for dust, polluted continental, and marine aerosols).

689
690 **Data availability statement.** All data that support the findings of this study are publicly available.
691 The in-situ measurements at the ARM-SGP are available at
692 <https://www.arm.gov/capabilities/observatories/sgp>.

693 All ORACLES data are accessible via the digital object identifiers (DOIs) provided under
694 ORACLES science team.
695 references: https://doi.org/10.5067/Suborbital/ORACLES/P3/2018_V2 (ORACLES Science
696 Team, 2020a), https://doi.org/10.5067/Suborbital/ORACLES/P3/2017_V2 (ORACLES Science
697 Team, 2020b).

698 The CALIPSO data are available at <https://eosweb.larc.nasa.gov/>.

699
700 **Author contributions.** PNP conceptualized and designed the study. PNP carried out the data
701 analysis and interpretation with contributions from JHJ, RG and HG. PNP wrote the manuscript.
702 JHJ, RG, HG, OVK, MJG, LG, FX and OA reviewed, commented and/or edited the manuscript.

703 **Competing Interests:** The contact author has declared that none of the authors has any competing
704 interests.

705 **Acknowledgment.** This work was conducted at the NASA-sponsored Jet Propulsion Laboratory
706 (JPL), California Institute of Technology, under contract by NASA. We appreciate the facility
707 provided by the JPL for data analysis and research. This work was supported by the NASA
708 Postdoctoral Program, administered by Oak Ridge Associated Universities under contract with
709 NASA. We are thankful to Charles A. Brock (Chemical Sciences Laboratory, National Oceanic and
710 Atmospheric Administration, Boulder, CO, USA) for the fruitful discussion on the present study. All
711 data were obtained from the Atmospheric Radiation Measurement (ARM) Program sponsored by
712 the U.S. Department of Energy, Office of Science, Office of Biological and Environmental
713 Research, Climate and Environmental Sciences Division, and National Science Foundation. We



714 thank the ORACLES deployment support teams and the science team for a successful and
715 productive mission. We thank the CALIPSO science team, for providing the CALIPSO data.

716

717 References

- 718 Andreae, M. O., & Rosenfeld, D. (2008). Aerosol-cloud-precipitation interactions. Part 1. The
719 nature and sources of cloud-active aerosols. *Earth-Science Reviews*, 89(1–2), 13–41.
720 <https://doi.org/10.1016/j.earscirev.2008.03.001>
- 721 Bedoya-Velásquez, A. E., Navas-Guzmán, F., Granados-Muñoz, M. J., Titos, G., Román, R.,
722 Andrés Casquero-Vera, J., Ortiz-Amezcuca, P., Antonio Benavent-Oltra, J., de Arruda
723 Moreira, G., Montilla-Rosero, E., Hoyos, C. D., Artiñano, B., Coz, E., Olmo-Reyes, F. J.,
724 Alados-Arboledas, L., & Guerrero-Rascado, J. L. (2018). Hygroscopic growth study in the
725 framework of EARLINET during the SLOPE i campaign: Synergy of remote sensing and in
726 situ instrumentation. *Atmospheric Chemistry and Physics*, 18(10), 7001–7017.
727 <https://doi.org/10.5194/ACP-18-7001-2018>
- 728 Bi, L., Yang, P., Kattawar, G. W., & Kahn, R. (2009). Single-scattering properties of triaxial
729 ellipsoidal particles for a size parameter range from the Rayleigh to geometric-optics
730 regimes. *Applied Optics*, 48(1), 114–126. <https://doi.org/10.1364/AO.48.000114>
- 731 Bohren, C. F., & Huffman, D. R. (1998). Absorption and Scattering of Light by Small Particles.
732 *Absorption and Scattering of Light by Small Particles*.
733 <https://doi.org/10.1002/9783527618156>
- 734 Braun, S., Stephens, G., Berndt, E., Blanchard, Y., Blanchet, J.-P., Carmichael, G., da Silva, A.,
735 Ferrare, R., Ivanco, M., Kacenelenbogen, M., Kirschbaum, D., Libois, Q., Mace, G., Omar,
736 A., Petersen, W., Redemann, J., Seidel, F., van den Heever, S., Waliser, D., & Winker, D.
737 (2022). *Aerosol, Cloud, Convection, and Precipitation (ACCP) Science & Applications*.
738 [https://aos.gsfc.nasa.gov/docs/ACCP_Science_Narrative-\(Mar2022\).pdf](https://aos.gsfc.nasa.gov/docs/ACCP_Science_Narrative-(Mar2022).pdf)
- 739 Brock, C. A., Wagner, N. L., Anderson, B. E., Attwood, A. R., Beyersdorf, A., Campuzano-Jost,
740 P., Carlton, A. G., Day, D. A., Diskin, G. S., Gordon, T. D., Jimenez, J. L., Lack, D. A.,
741 Liao, J., Markovic, M. Z., Middlebrook, A. M., Ng, N. L., Perring, A. E., Richardson, M.
742 S., Schwarz, J. P., ... Murphy, D. M. (2016). Aerosol optical properties in the southeastern
743 United States in summer - Part 1: Hygroscopic growth. *Atmospheric Chemistry and Physics*,
744 16(8), 4987–5007. <https://doi.org/10.5194/ACP-16-4987-2016>
- 745 Burkart, J., Steiner, G., Reischl, G., & Hitzemberger, R. (2011). Long-term study of cloud
746 condensation nuclei (CCN) activation of the atmospheric aerosol in Vienna. *Atmospheric
747 Environment*, 45(32), 5751–5759. <https://doi.org/10.1016/J.ATMOSENV.2011.07.022>
- 748 Burton, S. P., Chemyakin, E., Liu, X., Knobelspiesse, K., Stamnes, S., Sawamura, P., Moore, R.
749 H., Hostetler, C. A., & Ferrare, R. A. (2016). Information content and sensitivity of the 3β +



- 750 2 α lidar measurement system for aerosol microphysical retrievals. *Atmospheric*
751 *Measurement Techniques*, 9(11), 5555–5574. <https://doi.org/10.5194/AMT-9-5555-2016>
- 752 Burton, S. P., Ferrare, R. A., Hostetler, C. A., Hair, J. W., Rogers, R. R., Obland, M. D., Butler,
753 C. F., Cook, A. L., Harper, D. B., & Froyd, K. D. (2012). Aerosol classification using
754 airborne High Spectral Resolution Lidar measurements-methodology and examples.
755 *Atmospheric Measurement Techniques*, 5(1), 73–98. [https://doi.org/10.5194/AMT-5-73-](https://doi.org/10.5194/AMT-5-73-2012)
756 2012
- 757 Carslaw, K. S., Boucher, O., Spracklen, D. v., Mann, G. W., L. Rae, J. G., Woodward, S., &
758 Kulmala, M. (2010). A review of natural aerosol interactions and feedbacks within the Earth
759 system. *Atmospheric Chemistry and Physics*, 10(4), 1701–1737.
760 <https://doi.org/10.5194/ACP-10-1701-2010>
- 761 Chemyakin, E., Burton, S., Kolgotin, A., Müller, D., Hostetler, C., & Ferrare, R. (2016).
762 Retrieval of aerosol parameters from multiwavelength lidar: investigation of the underlying
763 inverse mathematical problem. *Applied Optics*, 55(9), 2188.
764 <https://doi.org/10.1364/AO.55.002188>
- 765 Choudhury, G., & Tesche, M. (2022). Estimating cloud condensation nuclei concentrations from
766 CALIPSO lidar measurements. *Atmospheric Measurement Techniques*, 15(3), 639–654.
767 <https://doi.org/10.5194/AMT-15-639-2022>
- 768 Clarke, A., & Kapustin, V. (2010). Hemispheric aerosol vertical profiles: Anthropogenic impacts
769 on optical depth and cloud nuclei. *Science*, 329(5998), 1488–1492.
770 https://doi.org/10.1126/SCIENCE.1188838/SUPPL_FILE/CLARKE.SOM.PDF
- 771 Dubovik, O. (2002). Variability of absorption and optical properties of key aerosol types
772 observed in worldwide locations. *J. Atmos. Sci.*, 59, 590–608. [https://doi.org/10.1175/1520-](https://doi.org/10.1175/1520-0469(2002)059<0590:voaaop>2.0.co)
773 0469(2002)059<0590:voaaop>2.0.co
- 774 Dubovik, O., Sinyuk, A., Lapyonok, T., Holben, B. N., Mishchenko, M., Yang, P., Eck, T. F.,
775 Volten, H., Muñoz, O., Veihelmann, B., van der Zande, W. J., Leon, J. F., Sorokin, M., &
776 Slutsker, I. (2006). Application of spheroid models to account for aerosol particle
777 nonsphericity in remote sensing of desert dust. *Journal of Geophysical Research*
778 *Atmospheres*, 111(11). <https://doi.org/10.1029/2005JD006619>
- 779 Dusek, U., Frank, G. P., Hildebrandt, L., Curtius, J., Schneider, J., Walter, S., Chand, D.,
780 Drewnick, F., Hings, S., Jung, D., Borrmann, S., & Andreae, M. O. (2006). Size matters
781 more than chemistry for cloud-nucleating ability of aerosol particles. *Science*.
782 <https://doi.org/10.1126/science.1125261>
- 783 Fan, J., Wang, Y., Rosenfeld, D., & Liu, X. (2016). Review of Aerosol–Cloud Interactions:
784 Mechanisms, Significance, and Challenges. *Journal of the Atmospheric Sciences*, 73(11),
785 4221–4252. <https://doi.org/10.1175/JAS-D-16-0037.1>
- 786 Feingold, G., Yang, S., Hardesty, R. M., & Cotton, W. R. (1998). Feasibility of retrieving cloud
787 condensation nucleus properties from doppler cloud radar, microwave radiometer, and lidar.



- 788 *Journal of Atmospheric and Oceanic Technology*. [https://doi.org/10.1175/1520-](https://doi.org/10.1175/1520-0426(1998)015<1188:FORCCN>2.0.CO;2)
789 0426(1998)015<1188:FORCCN>2.0.CO;2
- 790 Fernández, A. J., Molero, F., Becerril-Valle, M., Coz, E., Salvador, P., Artíñano, B., & Pujadas,
791 M. (2018). Application of remote sensing techniques to study aerosol water vapour uptake
792 in a real atmosphere. *Atmospheric Research*, 202, 112–127.
793 <https://doi.org/10.1016/J.ATMOSRES.2017.11.020>
- 794 Ghan, S. J., & Collins, D. R. (2004). Use of in situ data to test a Raman lidar-based cloud
795 condensation nuclei remote sensing method. *Journal of Atmospheric and Oceanic*
796 *Technology*. [https://doi.org/10.1175/1520-0426\(2004\)021<0387:UOISDT>2.0.CO;2](https://doi.org/10.1175/1520-0426(2004)021<0387:UOISDT>2.0.CO;2)
- 797 Ghan, S. J., Rissman, T. A., Elleman, R., Ferrare, R. A., Turner, D., Flynn, C., Wang, J., Orgen,
798 J., Hudson, J., Jonsson, H. H., VanReken, T., Flagan, R. C., & Seinfeld, J. H. (2006). Use of
799 situ cloud condensation nuclei, extinction, and aerosol size distribution measurements to
800 test a method for retrieving cloud condensation nuclei profiles from surface measurements.
801 *Journal of Geophysical Research Atmospheres*, 111(5).
802 <https://doi.org/10.1029/2004JD005752>
- 803 Gryspeerdt, E., & Stier, P. (2012). Regime-based analysis of aerosol-cloud interactions.
804 *Geophysical Research Letters*. <https://doi.org/10.1029/2012GL053221>
- 805 Hatch, T., & Choate, S. P. (1929). Statistical description of the size properties of non uniform
806 particulate substances. *Journal of the Franklin Institute*, 207(3), 369–387.
807 [https://doi.org/10.1016/S0016-0032\(29\)91451-4](https://doi.org/10.1016/S0016-0032(29)91451-4)
- 808 IPCC. (2013). Working Group I Contribution to the IPCC Fifth Assessment Report, Climate
809 Change 2013: The Physical Science Basis. *Ippc, AR5*(March 2013), 2014.
810 <https://doi.org/10.1017/CBO9781107415324.Summary>
- 811 IPCC. (2014). Climate Change 2014: Synthesis Report. Contribution of Working Groups I, II
812 and III to the Fifth Assessment Report of the Intergovernmental Panel on Climate Change.
813 In *Core Writing Team, R.K. Pachauri and L.A. Meyer*. IPCC.
814 <https://doi.org/10.1017/CBO9781107415324.004>
- 815 Jurányi, Z., Gysel, M., Weingartner, E., Decarlo, P. F., Kammermann, L., & Baltensperger, U.
816 (2010). Measured and modelled cloud condensation nuclei number concentration at the high
817 alpine site Jungfraujoch. *Atmospheric Chemistry and Physics*, 10(16), 7891–7906.
818 <https://doi.org/10.5194/ACP-10-7891-2010>
- 819 Kantorovitch, L. (1939). The method of successive approximation for functional equations. *Acta*
820 *Mathematica*, 71(1), 63–97. <https://doi.org/10.1007/BF02547750>
- 821 Kapustin, V. N., Clarke, A. D., Shinozuka, Y., Howell, S., Brekhovskikh, V., Nakajima, T., &
822 Higurashi, A. (2006). On the determination of a cloud condensation nuclei from satellite:
823 Challenges and possibilities. *Journal of Geophysical Research Atmospheres*.
824 <https://doi.org/10.1029/2004JD005527>



- 825 Kasten, F. (1969). Visibility forecast in the phase of pre-condensation. *Tellus*, 21(5), 631–635.
826 <https://doi.org/10.3402/TELLUSA.V21I5.10112>
- 827 Koehler, K. A., Kreidenweis, S. M., DeMott, P. J., Petters, M. D., Prenni, A. J., & Carrico, C. M.
828 (2009). Hygroscopicity and cloud droplet activation of mineral dust aerosol. *Geophysical*
829 *Research Letters*, 36(8). <https://doi.org/10.1029/2009GL037348>
- 830 Kolmogorov, A. N. (1941). About the Logarithmic-normal Law of Particle Size Distribution
831 during Crushing. *Proceedings of the USSR Academy of Sciences*, 31(2), 99–101.
- 832 Kuang, Y., Zhao, C., Tao, J., Bian, Y., Ma, N., & Zhao, G. (2017). A novel method for deriving
833 the aerosol hygroscopicity parameter based only on measurements from a humidified
834 nephelometer system. *Atmospheric Chemistry and Physics*, 17(11), 6651–6662.
835 <https://doi.org/10.5194/ACP-17-6651-2017>
- 836 Li, J., Liu, X., Yuan, L., Yin, Y., Li, Z., Li, P., Ren, G., Jin, L., Li, R., Dong, Z., Li, Y., & Yang,
837 J. (2015). Vertical distribution of aerosol optical properties based on aircraft measurements
838 over the Loess Plateau in China. *Journal of Environmental Sciences (China)*, 34, 44–56.
839 <https://doi.org/10.1016/J.JES.2015.01.021>
- 840 Li, J., Yin, Y., Li, P., Li, Z., Li, R., Cribb, M., Dong, Z., Zhang, F., Li, J., Ren, G., Jin, L., & Li,
841 Y. (2015). Aircraft measurements of the vertical distribution and activation property of
842 aerosol particles over the Loess Plateau in China. *Atmospheric Research*, 155, 73–86.
843 <https://doi.org/10.1016/J.ATMOSRES.2014.12.004>
- 844 Liu, J., & Li, Z. (2014). Estimation of cloud condensation nuclei concentration from aerosol
845 optical quantities: Influential factors and uncertainties. *Atmospheric Chemistry and Physics*,
846 14(1), 471–483. <https://doi.org/10.5194/ACP-14-471-2014>
- 847 Liu, P. F., Zhao, C. S., Göbel, T., Hallbauer, E., Nowak, A., Ran, L., Xu, W. Y., Deng, Z. Z.,
848 Ma, N., Mildenerger, K., Henning, S., Stratmann, F., & Wiedensohler, A. (2011).
849 Hygroscopic properties of aerosol particles at high relative humidity and their diurnal
850 variations in the north China plain. *Atmospheric Chemistry and Physics*, 11(7), 3479–3494.
851 <https://doi.org/10.5194/ACP-11-3479-2011>
- 852 Lv, M., Liu, D., Li, Z., Mao, J., Sun, Y., Wang, Z., Wang, Y., & Xie, C. (2017). Hygroscopic
853 growth of atmospheric aerosol particles based on lidar, radiosonde, and in situ
854 measurements: Case studies from the Xinzhou field campaign. *Journal of Quantitative*
855 *Spectroscopy and Radiative Transfer*, 188, 60–70.
856 <https://doi.org/10.1016/J.QSRT.2015.12.029>
- 857 Lv, M., Wang, Z., Li, Z., Luo, T., Ferrare, R., Liu, D., Wu, D., Mao, J., Wan, B., Zhang, F., &
858 Wang, Y. (2018). Retrieval of Cloud Condensation Nuclei Number Concentration Profiles
859 From Lidar Extinction and Backscatter Data. *Journal of Geophysical Research:*
860 *Atmospheres*, 123(11), 6082–6098. <https://doi.org/10.1029/2017JD028102>



- 861 Mamouri, R. E., & Ansmann, A. (2016). Potential of polarization lidar to provide profiles of
862 CCN-and INP-relevant aerosol parameters. *Atmospheric Chemistry and Physics*, 16(9),
863 5905–5931. <https://doi.org/10.5194/acp-16-5905-2016>
- 864 Mattis, I., D'Amico, G., Baars, H., Amodeo, A., Madonna, F., & Iarlori, M. (2016). EARLINET
865 Single Calculus Chain - Technical - Part 2: Calculation of optical products. *Atmospheric
866 Measurement Techniques*, 9(7), 3009–3029. <https://doi.org/10.5194/AMT-9-3009-2016>
- 867 Mishchenko, M. I., & Travis, L. D. (1998). Capabilities and limitations of a current FORTRAN
868 implementation of the T-matrix method for randomly oriented, rotationally symmetric
869 scatterers. *Journal of Quantitative Spectroscopy and Radiative Transfer*, 60(3), 309–324.
870 [https://doi.org/10.1016/S0022-4073\(98\)00008-9](https://doi.org/10.1016/S0022-4073(98)00008-9)
- 871 Paasonen, P., Asmi, A., Petäjä, T., Kajos, M. K., Äijälä, M., Junninen, H., Holst, T., Abbatt, J. P.
872 D., Arneth, A., Birmili, W., van der Gon, H. D., Hamed, A., Hoffer, A., Laakso, L.,
873 Laaksonen, A., Richard Leitch, W., Plass-Dülmer, C., Pryor, S. C., Räisänen, P., ...
874 Kulmala, M. (2013). Warming-induced increase in aerosol number concentration likely to
875 moderate climate change. *Nature Geoscience*, 6(6), 438–442.
876 <https://doi.org/10.1038/NNGEO1800>
- 877 Patel, P. N., Gautam, R., Michibata, T., & Gadhavi, H. (2019). Strengthened Indian Summer
878 Monsoon Precipitation Susceptibility Linked to Dust-Induced Ice Cloud Modification.
879 *Geophysical Research Letters*, 46(14), 8431–8441. <https://doi.org/10.1029/2018GL081634>
- 880 Patel, P. N., & Jiang, J. H. (2021). Cloud condensation nuclei characteristics at the Southern
881 Great Plains site: role of particle size distribution and aerosol hygroscopicity.
882 *Environmental Research Communications*, 3(7), 075002. <https://doi.org/10.1088/2515-7620/AC0E0B>
883
- 884 Patel, P. N., & Kumar, R. (2016). Dust Induced Changes in Ice Cloud and Cloud Radiative
885 Forcing over a High Altitude Site. *Aerosol and Air Quality Research*, 16(8), 1820–1831.
886 <https://doi.org/10.4209/aaqr.2015.05.0325>
- 887 Patel, P. N., Quaas, J., & Kumar, R. (2017). A new statistical approach to improve the satellite-
888 based estimation of the radiative forcing by aerosol–cloud interactions. *Atmospheric
889 Chemistry and Physics*, 17(5), 3687–3698. <https://doi.org/10.5194/acp-17-3687-2017>
- 890 Petters, M. D., Carrico, C. M., Kreidenweis, S. M., Prenni, A. J., DeMott, P. J., Collett, J. L., &
891 Moosmüller, H. (2009). Cloud condensation nucleation activity of biomass burning aerosol.
892 *Journal of Geophysical Research Atmospheres*, 114(22), 1–16.
893 <https://doi.org/10.1029/2009JD012353>
- 894 Petters, M. D., & Kreidenweis, S. M. (2007). A single parameter representation of hygroscopic
895 growth and cloud condensation nucleus activity. *Atmospheric Chemistry and Physics*, 7(8),
896 1961–1971. <https://doi.org/10.5194/ACP-7-1961-2007>



- 897 Quaas, J., Boucher, O., Bellouin, N., & Kinne, S. (2008). Satellite-based estimate of the direct
898 and indirect aerosol climate forcing. *Journal of Geophysical Research Atmospheres*, 113(5).
899 <https://doi.org/10.1029/2007JD008962>
- 900 Quaas, J., Ming, Y., Menon, S., Takemura, T., Wang, M., Penner, J. E., Gettelman, A.,
901 Lohmann, U., Bellouin, N., Boucher, O., Sayer, A. M., Thomas, G. E., McComiskey, A.,
902 Feingold, G., Hoose, C., Kristjánsson, J. E., Liu, X., Balkanski, Y., Donner, L. J., ...
903 Schulz, M. (2009). Aerosol indirect effects - general circulation model intercomparison and
904 evaluation with satellite data. *Atmospheric Chemistry and Physics*, 9(22), 8697–8717.
905 <https://doi.org/10.5194/acp-9-8697-2009>
- 906 Redemann, J., Wood, R., Zuidema, P., Doherty, S. J., Luna, B., LeBlanc, S. E., Diamond, M. S.,
907 Shinozuka, Y., Chang, I. Y., Ueyama, R., Pfister, L., Ryoo, J. M., Dobracki, A. N., da Silva,
908 A. M., Longo, K. M., Kacenenbogen, M. S., Flynn, C. J., Pistone, K., Knox, N. M., ...
909 Gao, L. (2021). An overview of the ORACLES (ObseRvations of Aerosols above CLouds
910 and their intERactionS) project: aerosol-cloud-radiation interactions in the Southeast
911 Atlantic basin. *Atmos. Chem. Phys.*, 21(3), 1507–1563. [https://doi.org/10.5194/acp-21-](https://doi.org/10.5194/acp-21-1507-2021)
912 [1507-2021](https://doi.org/10.5194/acp-21-1507-2021)
- 913 Rosenfeld, D. (2008). Flood or drought: how do aerosols affect precipitation? *Science*, 321,
914 1309–1313.
- 915 Rosenfeld, D., Andreae, M. O., Asmi, A., Chin, M., Leeuw, G., Donovan, D. P., Kahn, R.,
916 Kinne, S., Kivekäs, N., Kulmala, M., Lau, W., Schmidt, K. S., Suni, T., Wagner, T., Wild,
917 M., & Quaas, J. (2014). Global observations of aerosol-cloud-precipitation- climate
918 interactions. *Rev. Geophys.*, 52, 750–808. <https://doi.org/10.1002/2013RG000441>
- 919 Rosenfeld, D., Zheng, Y., Hashimshoni, E., Pöhlker, M. L., Jefferson, A., Pöhlker, C., Yu, X.,
920 Zhu, Y., Liu, G., Yue, Z., Fischman, B., Li, Z., Giguzin, D., Goren, T., Artaxo, P., Barbosa,
921 H. M. J., Pöschl, U., & Andreae, M. O. (2016). Satellite retrieval of cloud condensation
922 nuclei concentrations by using clouds as CCN chambers. *Proceedings of the National*
923 *Academy of Sciences*. <https://doi.org/10.1073/pnas.1514044113>
- 924 Seinfeld, J. H., Bretherton, C., Carslaw, K. S., Coe, H., DeMott, P. J., Dunlea, E. J., Feingold, G.,
925 Ghan, S., Guenther, A. B., Kahn, R., Kraucunas, I., Kreidenweis, S. M., Molina, M. J.,
926 Nenes, A., Penner, J. E., Prather, K. A., Ramanathan, V., Ramaswamy, V., Rasch, P. J., ...
927 Wood, R. (2016). Improving our fundamental understanding of the role of aerosol–cloud
928 interactions in the climate system. *Proceedings of the National Academy of Sciences*,
929 113(21), 5781–5790. <https://doi.org/10.1073/pnas.1514043113>
- 930 Shinozuka, Y., Clarke, A. D., Nenes, A., Jefferson, A., Wood, R., McNaughton, C. S., Ström, J.,
931 Tunved, P., Redemann, J., Thornhill, K. L., Moore, R. H., Latham, T. L., Lin, J. J., & Yoon,
932 Y. J. (2015). The relationship between cloud condensation nuclei (CCN) concentration and
933 light extinction of dried particles: Indications of underlying aerosol processes and
934 implications for satellite-based CCN estimates. *Atmospheric Chemistry and Physics*, 15(13),
935 7585–7604. <https://doi.org/10.5194/ACP-15-7585-2015>



- 936 Stier, P. (2016). Limitations of passive remote sensing to constrain global cloud condensation
937 nuclei. *Atmospheric Chemistry and Physics*, 16(10), 6595–6607.
938 <https://doi.org/10.5194/ACP-16-6595-2016>
- 939 Tan, W., Zhao, G., Yu, Y., Li, C., Li, J., Kang, L., Zhu, T., & Zhao, C. (2019). Method to
940 retrieve cloud condensation nuclei number concentrations using lidar measurements.
941 *Atmospheric Measurement Techniques*, 12(7), 3825–3839. [https://doi.org/10.5194/AMT-](https://doi.org/10.5194/AMT-12-3825-2019)
942 [12-3825-2019](https://doi.org/10.5194/AMT-12-3825-2019)
- 943 Tesche, M., Ansmann, A., Müller, D., Althausen, D., Engelmann, R., Freudenthaler, V., & Groß,
944 S. (2009). Vertically resolved separation of dust and smoke over Cape Verde using
945 multiwavelength Raman and polarization lidars during Saharan Mineral Dust Experiment
946 2008. *Journal of Geophysical Research Atmospheres*, 114(13).
947 <https://doi.org/10.1029/2009JD011862>
- 948 Titos, G., Cazorla, A., Zieger, P., Andrews, E., Lyamani, H., Granados-Muñoz, M. J., Olmo, F.
949 J., & Alados-Arboledas, L. (2016). Effect of hygroscopic growth on the aerosol light-
950 scattering coefficient: A review of measurements, techniques and error sources.
951 *Atmospheric Environment*, 141, 494–507.
952 <https://doi.org/10.1016/J.ATMOSENV.2016.07.021>
- 953 Torres, B., Dubovik, O., Fuertes, D., Schuster, G., Eugenia Cachorro, V., Lapyonok, T., Goloub,
954 P., Blarel, L., Barreto, A., Mallet, M., Toledano, C., & Tanré, D. (2017). Advanced
955 characterisation of aerosol size properties from measurements of spectral optical depth
956 using the GRASP algorithm. *Atmospheric Measurement Techniques*, 10(10), 3743–3781.
957 <https://doi.org/10.5194/AMT-10-3743-2017>
- 958 Wang, Y., Li, Z., Zhang, Y., Du, W., Zhang, F., Tan, H., Xu, H., Fan, T., Jin, X., Fan, X., Dong,
959 Z., Wang, Q., & Sun, Y. (2018). Characterization of aerosol hygroscopicity, mixing state,
960 and CCN activity at a suburban site in the central North China Plain. *Atmospheric*
961 *Chemistry and Physics*, 18(16), 11739–11752. <https://doi.org/10.5194/acp-18-11739-2018>
- 962 Xu, F., Gao, L., Redemann, J., Flynn, C. J., Espinosa, W. R., da Silva, A. M., Stamnes, S.,
963 Burton, S. P., Liu, X., Ferrare, R., Cairns, B., & Dubovik, O. (2021). A Combined Lidar-
964 Polarimeter Inversion Approach for Aerosol Remote Sensing Over Ocean. *Frontiers in*
965 *Remote Sensing*, 0, 2. <https://doi.org/10.3389/FRSEN.2021.620871>
- 966 Yang, P., Feng, Q., Hong, G., Kattawar, G. W., Wiscombe, W. J., Mishchenko, M. I., Dubovik,
967 O., Laszlo, I., & Sokolik, I. N. (2007). Modeling of the scattering and radiative properties of
968 nonspherical dust-like aerosols. *Journal of Aerosol Science*, 38(10), 995–1014.
969 <https://doi.org/10.1016/J.JAEROSCI.2007.07.001>
- 970
- 971



972

973 **Table 1:** CCN errors at six supersaturation (SS) retrieved from error-free inputs for the five
 974 aerosol types

Aerosol Types	CCN error (%)					
	0.07%	0.1%	0.2%	0.4%	0.8%	1.0%
Marine	-0.00 ± 0.21	-0.01 ± 0.23	0.00 ± 0.26	-0.00 ± 0.25	0.00 ± 0.23	-0.00 ± 0.24
Dust	-0.01 ± 0.22	-0.01 ± 0.23	0.00 ± 0.26	-0.01 ± 0.24	0.00 ± 0.25	-0.01 ± 0.23
Mean ± SD (%)						
Polluted continental	-0.01 ± 0.18	0.00 ± 0.18	-0.01 ± 0.16	0.00 ± 0.18	-0.01 ± 0.19	-0.00 ± 0.18
Clean continental	-0.01 ± 0.19	-0.01 ± 0.20	-0.01 ± 0.19	-0.00 ± 0.17	-0.00 ± 0.18	-0.01 ± 0.17
Smoke	-0.01 ± 0.19	-0.01 ± 0.21	-0.01 ± 0.18	-0.01 ± 0.20	-0.00 ± 0.22	-0.01 ± 0.19

975

976

977

978 **Table 2:** Sensitivity of CCN retrieval to the bimodal fits at different supersaturation ratios from
 979 the 100 aerosol size distributions obtained from ARM-SGP. The CCN error is calculated as an
 980 absolute value.

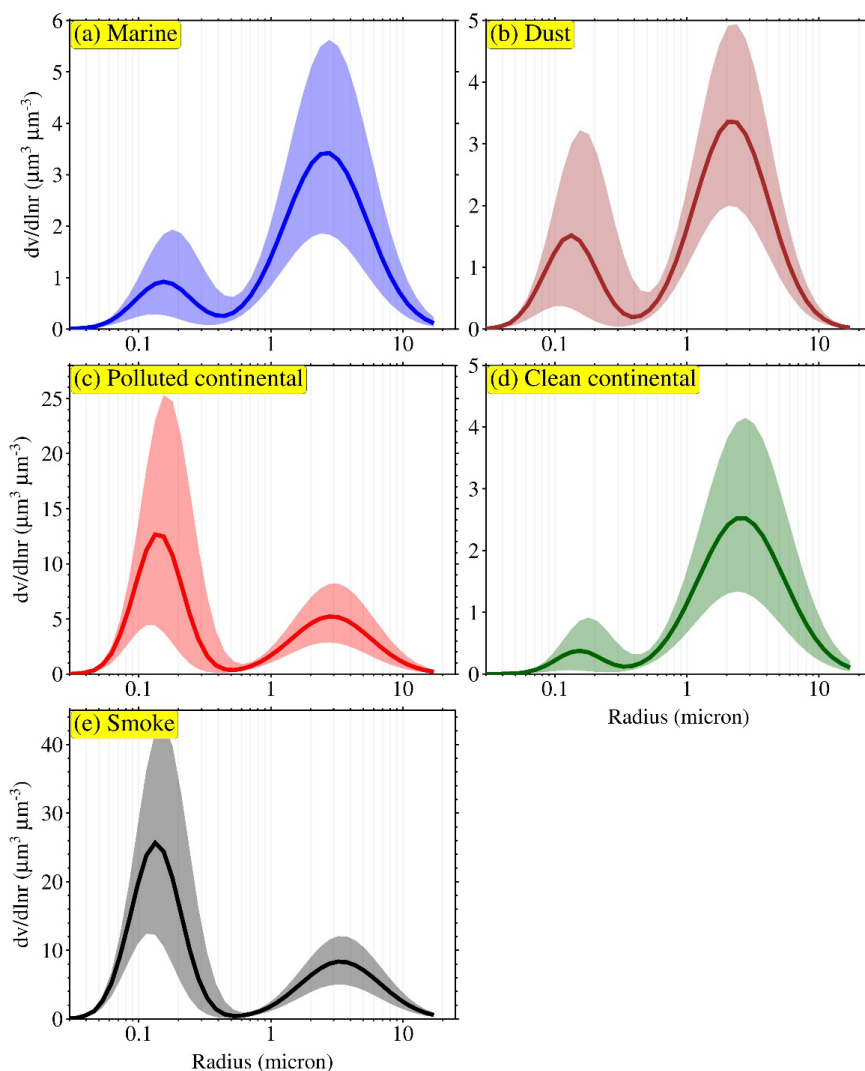
Mean ± SD (%)	CCN error (%)					
	0.07%	0.1%	0.2%	0.4%	0.8%	1.0%
	3.3 ± 2.4	3.9 ± 2.8	3.1 ± 2.7	2.9 ± 1.8	2.1 ± 1.5	1.7 ± 1.3

981

982



983

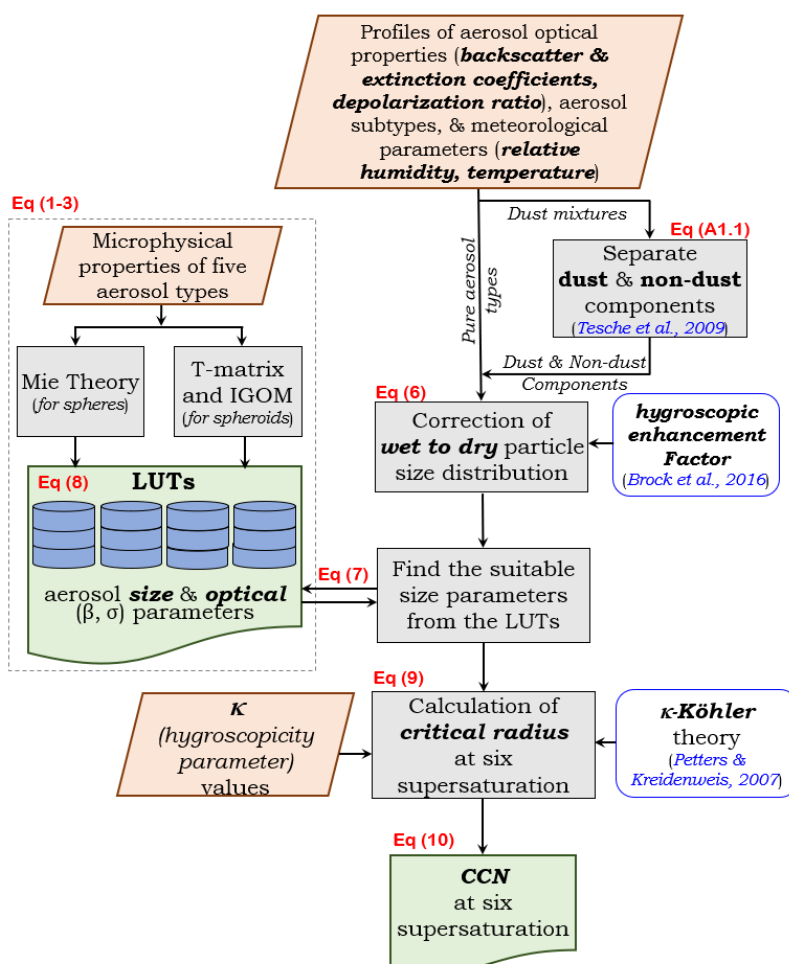


984

985 **Figure 1: Bimodal log-normal particle size distributions** for five aerosol types (marine, dust,
986 polluted continental, clean continental and smoke aerosols) considered in this study to build the
987 look-up-tables (LUTs). These particle size distributions were derived using measurements from
988 sun/sky radiometer at multiple selected Aerosol Robotic Network (AERONET) sites. Solid line
989 represents the mean of particle size distribution, whereas the shaded area shows the range of size
990 distribution covers in the respective LUTs.



991



992

993 **Figure 2: Flowchart of ECLiAP algorithm for the retrieval of N_{CCN} from lidar measurements.**

994 The steps within the dotted line box describes the pre-processing which includes the calculation

995 of aerosol optical properties using Mie scattering theory (T-matrix/IGOM for dust) to build look-

996 up-tables for five aerosol models. The steps outside the dotted line box represent the retrieval

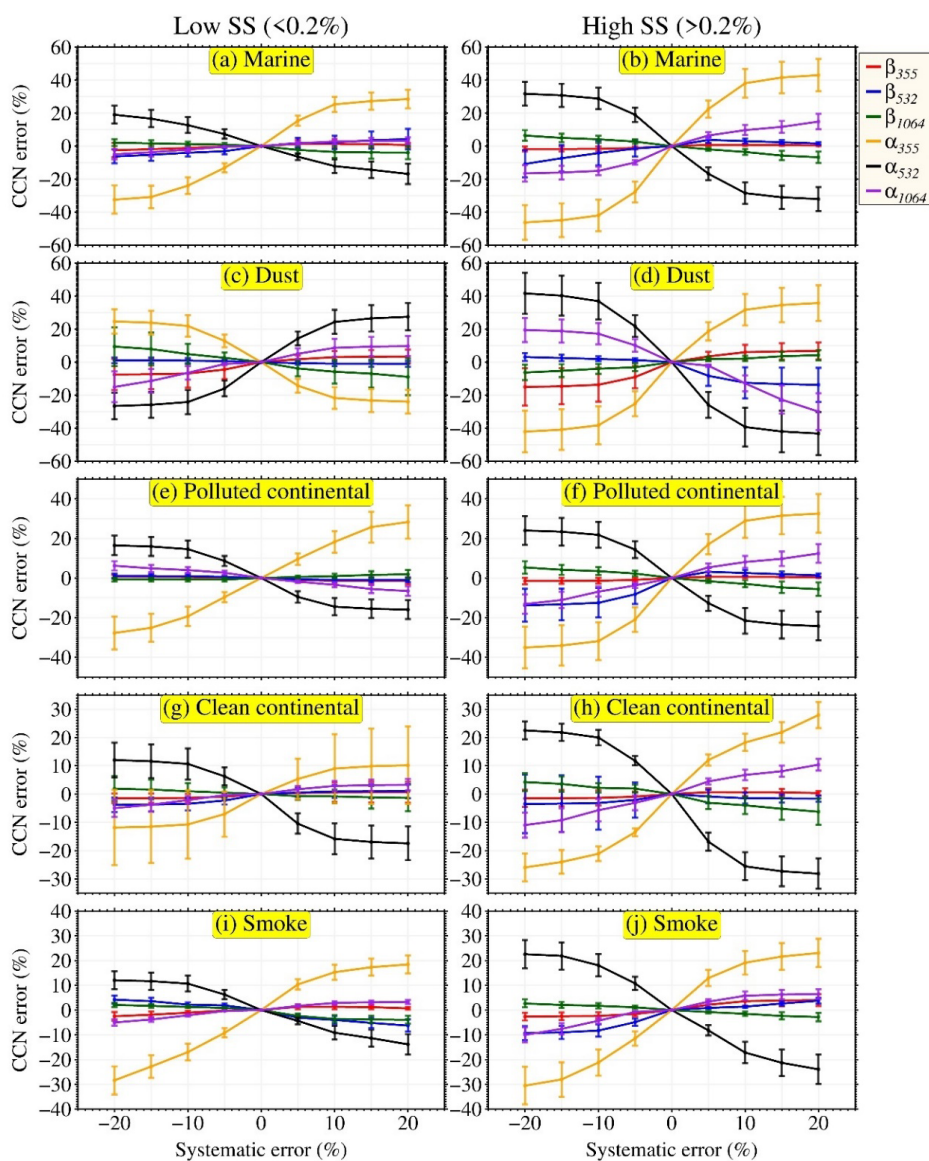
997 process of N_{CCN} from the given inputs of aerosol optical properties and meteorological

998 parameters. The chart also refers to the used equations associated to the particular retrieval

999 process.



1000



1001

1002

1003

1004

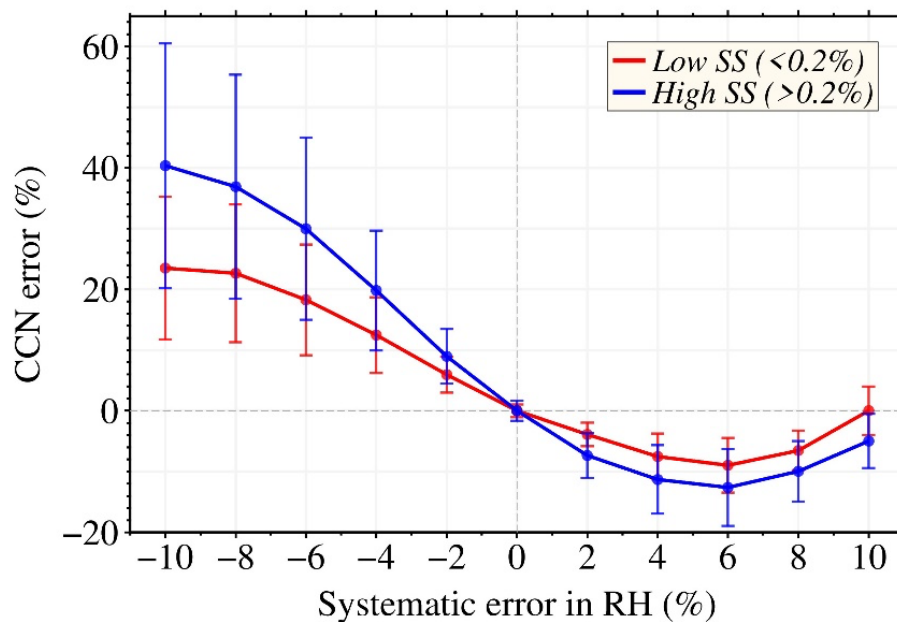
1005

Figure 3: Systematic errors in retrieved N_{CCN} . This represents the errors in retrieved N_{CCN} as a function of systematic errors in backscatter and extinction coefficients at all three wavelengths for low ($\leq 0.2\%$) and high ($> 0.2\%$) supersaturations and for all five aerosol subtypes as. The markers denote the mean value and the error bars represent the standard deviation.



1006

1007



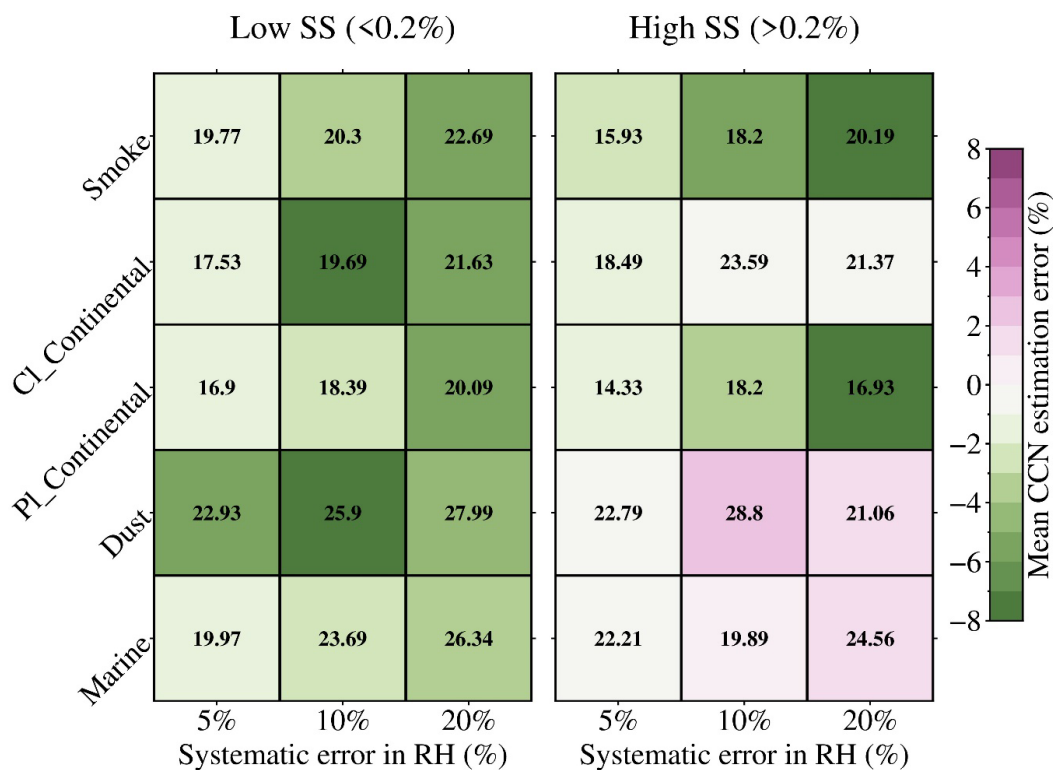
1008

1009 **Figure 4: Systematic errors in retrieved N_{CCN} .** This represent the errors in retrieved N_{CCN} as a
1010 function of systematic error in RH, combines for all aerosol subtypes, at low ($\leq 0.2\%$) and high
1011 ($> 0.2\%$) supersaturations. The markers denote the mean value and the error bars represent the
1012 standard deviation.



1013

1014



1015

1016

1017

1018

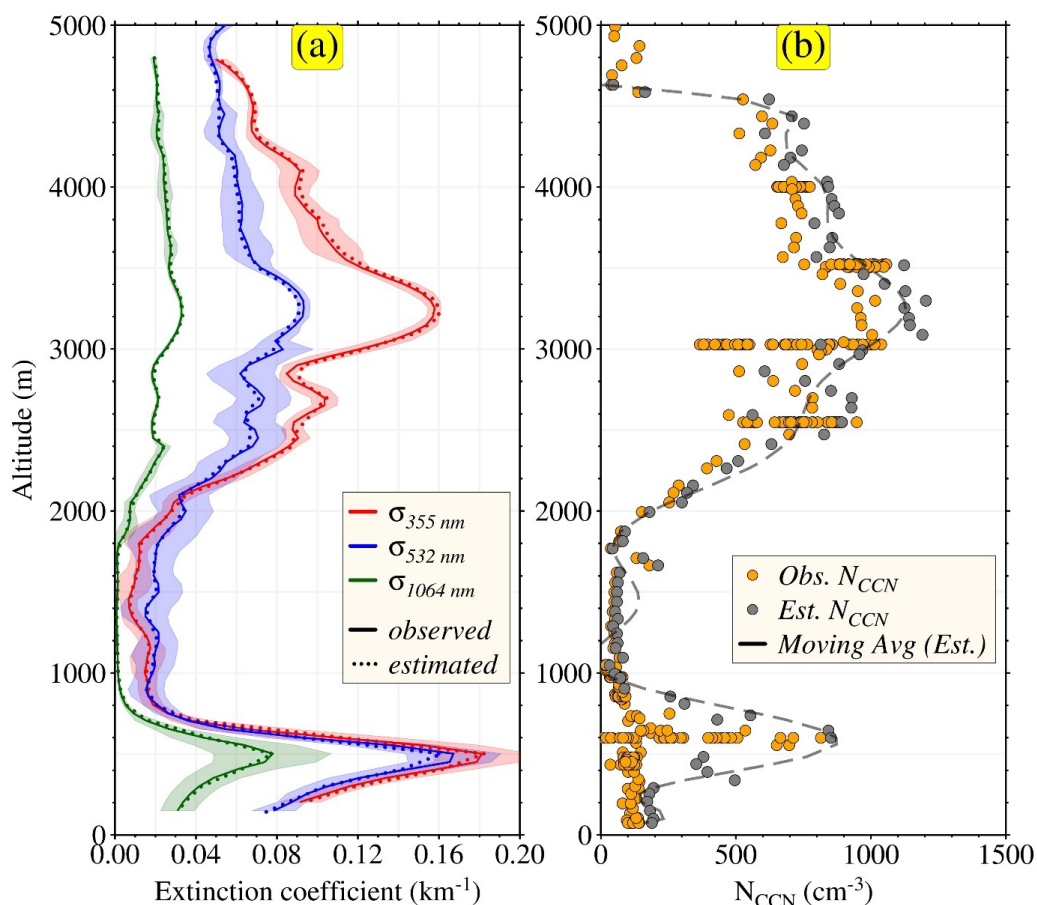
1019

1020

Figure 5: Random errors in retrieved N_{CCN} . This represent the random errors in retrieved N_{CCN} at low ($\leq 0.2\%$) and high ($> 0.2\%$) supersaturations with different random error conditions individually for five aerosol subtypes. The uncertainty of backscatter and extinction coefficients off all the tests is 10% and the uncertainties of RH are 5%, 10% and 20%. The color shows the mean values whereas number shows the ± 1 standard deviation of errors.



1021



1022

1023

1024

1025

1026

1027

1028

1029

1030

1031

1032

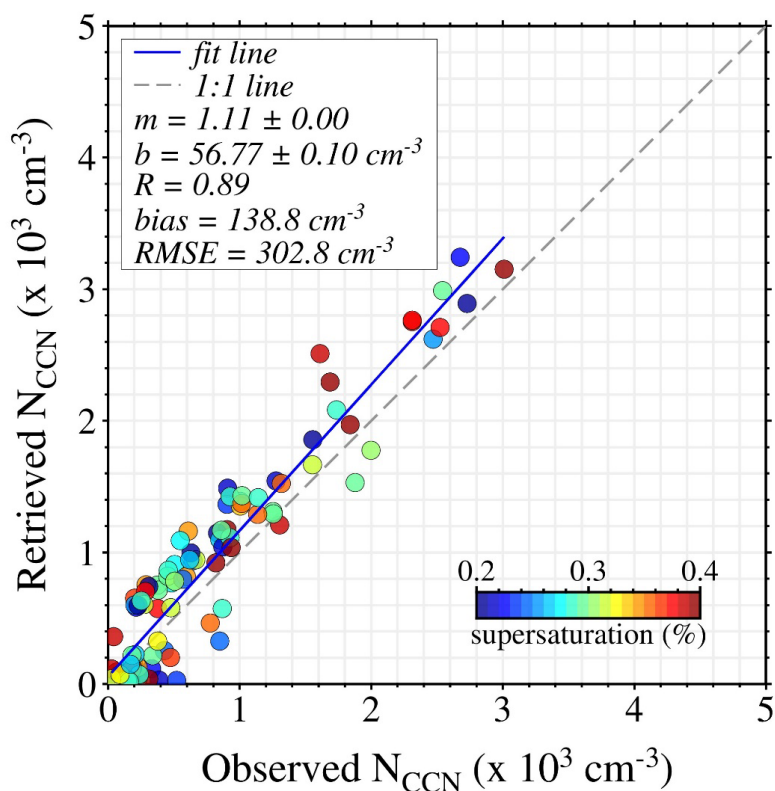
1033

Figure 6: Comparison between retrieved and observed vertical profiles of aerosol extinction coefficients and N_{CCN} . The ECLiAP retrieved (a) aerosol extinction coefficients at 355, 532 and 1064 nm and (b) N_{CCN} were compared against the one observed during NASA ORACLES airborne campaign. The lidar signals were mainly influenced by the mixture of smoke and dust or marine aerosols. The relationship between HSRL-2 measured aerosol extinction coefficients (solid lines) and retrieved (dotted line) by an algorithm in the left panel. The right panel illustrates the comparison of retrieved N_{CCN} using lidar measurements and measured by CCN counter. The dashed line in the right panel shows the moving average of retrieved N_{CCN} values. CCN counter measured N_{CCN} at supersaturation ranging from 0.32%-0.34% for the selected region (described in Figure S4), therefore, the retrieval of N_{CCN} was carried out at supersaturation of 0.34%.



1034

1035



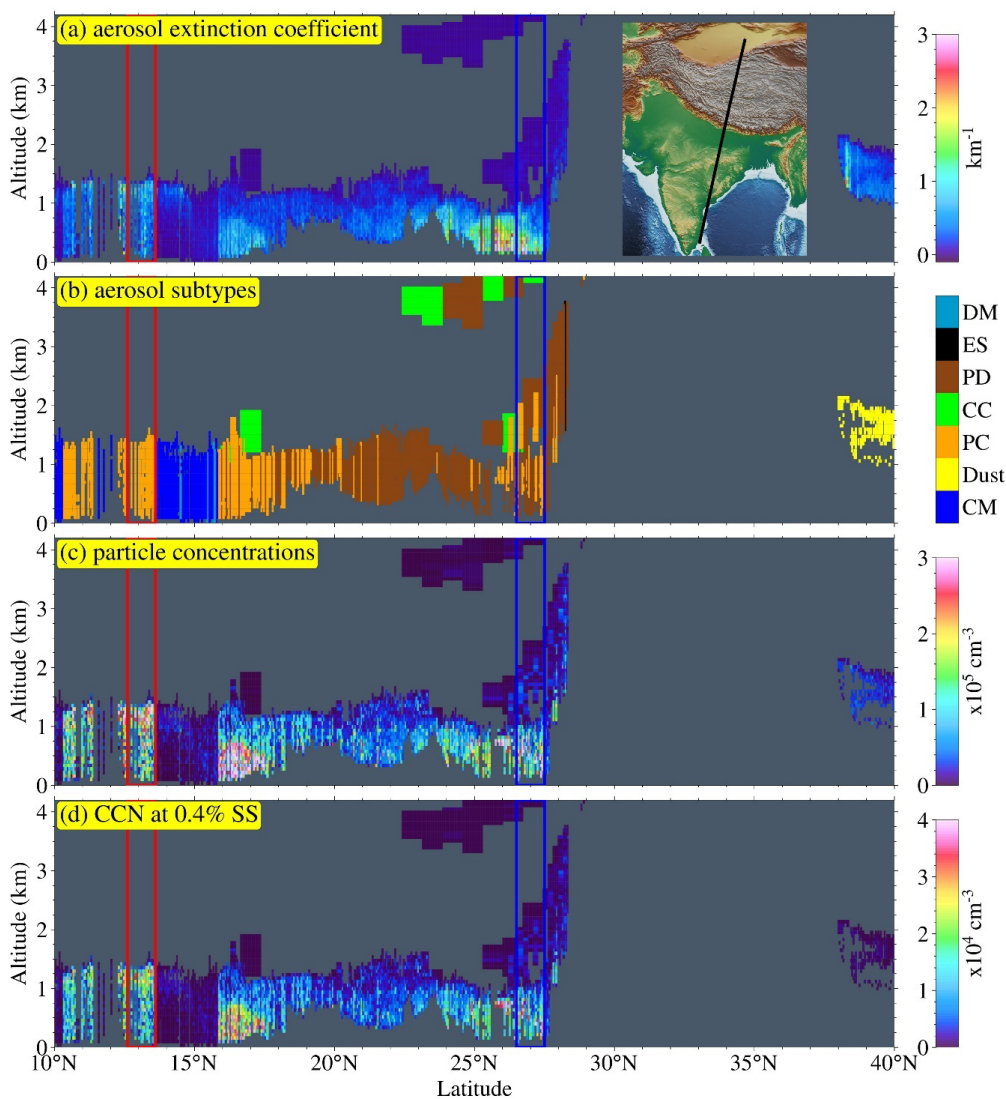
1036

1037 **Figure 7: Comparison between retrieved and observed N_{CCN} .** The comparison between ECLiAP
1038 retrieved N_{CCN} from HSRL-2 lidar measurements and the measured N_{CCN} values from CCN
1039 counter. The HSRL-2 and CCN counter data were collected from the multiple flights during NASA-
1040 ORACLES airborne campaigns conducted in 2017-2018. The color bar displays the observed
1041 values of supersaturation for each measurement and the N_{CCN} were retrieved on the same
1042 supersaturation for the direct comparison. The slope and intercept of the best fit line are given in
1043 the key by m and b , respectively. The gray dash line indicates the unit slope line and blue solid
1044 line indicates the regression line.

1045



1046



1047

1048

1049

1050

1051

1052

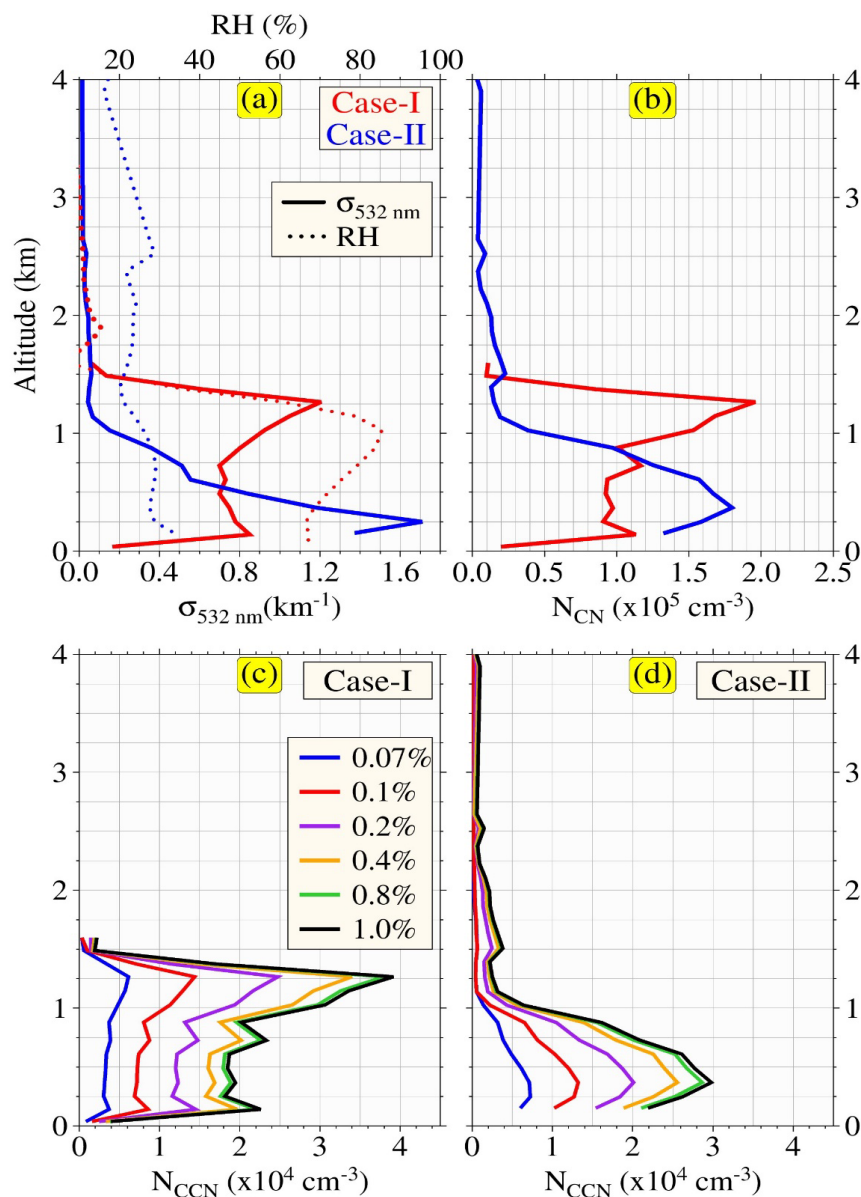
1053

1054

Figure 8: Retrieval from spaceborne lidar measurements. Explore the capability of ECLiAP, the N_{CN} , and N_{CCN} retrieved from CALIOP onboard CALIPSO observations on 01 January 2019, passing over the Tibetan plateau and Indian landmass. CALIOP derived (a) extinction coefficient at 532 nm, (b) aerosol subtypes were shown in the upper two panels. The lower two panels illustrate the ECLiAP retrieved (c) total particle concentrations (N_{CN}), and (d) N_{CCN} at supersaturation 0.4%. The two color boxes in red (case-I) and blue (case-II) are the two different scenarios that are further studied to assess the capability of ECLiAP.



1055



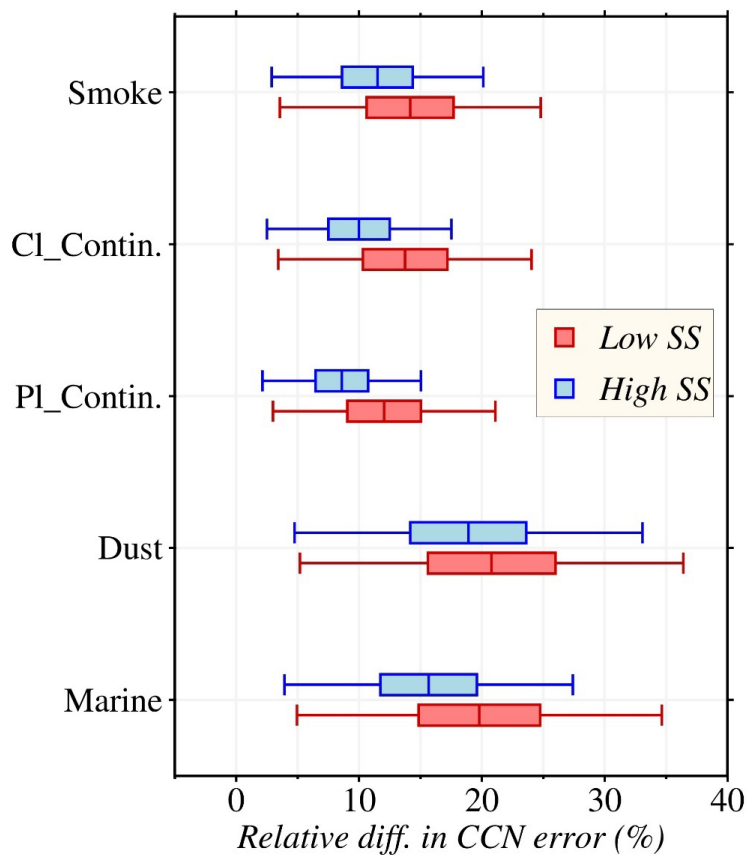
1056

1057 **Figure 9: Case studied from CALIOP observations.** As per mentioned above, two different
1058 scenarios (case-I dominated by polluted continental and case-II contains a mixture of polluted
1059 continental and polluted dust) were identified and studied in detail to assess the potential of
1060 ECLiAP to accurately capture the particles physicochemical characteristics and their influence
1061 on the retrieved values along with meteorological influence.



1062

1063



1064

1065 **Figure 10: Relative difference in CCN error between $3\beta+2\alpha$ and $3\beta+3\alpha$.** The CCN error were
1066 calculated against the given inputs using Eq. (11) for both the $3\beta+2\alpha$ and $3\beta+3\alpha$ techniques
1067 individually. Later the relative difference of CCN error has calculated from the individual CCN
1068 errors at low and high supersaturations for each aerosol subtypes.